

PAPER • OPEN ACCESS

Disentangling the effect of the hole-transporting layer, the bottom, and the top device on the fill factor in monolithic CIGSe-perovskite tandem solar cells by using spectroscopic and imaging tools

To cite this article: I Kafedjiska *et al* 2023 *J. Phys. Energy* **5** 024014

View the [article online](#) for updates and enhancements.

You may also like

- [The 2020 photovoltaic technologies roadmap](#)
Gregory M Wilson, Mowafak Al-Jassim, Wyatt K Metzger et al.
- [A transparent photovoltaic device of NiO/CdS arrays pn junction](#)
Wendi Fu, Jiaqi Pan and Chaorong Li
- [Design and simulation of different multilayer solar selective coatings for solar thermal applications](#)
Nahed El-Mahallawy, Mostafa R A Atia, Amany Khaled et al.



PAPER

OPEN ACCESS

RECEIVED
2 December 2022REVISED
19 February 2023ACCEPTED FOR PUBLICATION
8 March 2023PUBLISHED
4 April 2023Original Content from
this work may be used
under the terms of the
[Creative Commons
Attribution 4.0 licence](https://creativecommons.org/licenses/by/4.0/).Any further distribution
of this work must
maintain attribution to
the author(s) and the title
of the work, journal
citation and DOI.

Disentangling the effect of the hole-transporting layer, the bottom, and the top device on the fill factor in monolithic CIGSe-perovskite tandem solar cells by using spectroscopic and imaging tools

I Kafedjiska^{1,*} , G Farias Basulto¹ , F Ruske² , N Maticiu¹ , T Bertram¹ , C A Kaufmann¹ , R Schlatmann^{1,3} and I Lauer¹ ¹ Kompetenzzentrum Photovoltaik Berlin (PVcomB), Helmholtz-Zentrum Berlin für Materialien und Energie GmbH, Schwarzschildstraße 3, 12489 Berlin, Germany² Department Novel Materials and Interfaces for Photovoltaic Solar Cells, Helmholtz-Zentrum Berlin für Materialien und Energie GmbH, Kekuléstraße 5, 12489 Berlin, Germany³ Faculty 1 - Energy and Information, Hochschule für Technik und Wirtschaft, Berlin, Germany

* Author to whom any correspondence should be addressed.

E-mail: ivona.kafedjiska@helmholtz-berlin.de**Keywords:** monolithic CIGSe-perovskite tandem, morphological defect, ohmic shunt, dark lock-in thermography, X-ray/ultraviolet photoelectron spectroscopy (XPS/UPS), copper-doped nickel oxide (NiO_x:Cu), Fill Factor (FF)Supplementary material for this article is available [online](#)

Abstract

We present monolithic copper–indium–gallium–diselenide (Cu(In,Ga)Se₂, CIGSe)-perovskite tandem solar cells with air- or N₂-transferred NiO_x:Cu with or without self-assembled monolayer (SAM) as a hole-transporting layer (HTL). A champion efficiency of 23.2%, open-circuit voltage (V_{oc}) of 1.69 V, and a fill factor (FF) of 78.3% are achieved for the tandem with N₂-transferred NiO_x:Cu + SAM. The samples with air-transferred NiO_x:Cu + SAM have V_{oc} and FF losses, while those without SAM are heavily shunted. We find via x-ray and UV photoelectron spectroscopy that the air exposure leads to non-negligible loss in the Ni²⁺ species and changes in the NiO_x:Cu's work function and valence band maxima, both of which can negatively impact the V_{oc} and the FF of the tandems. Furthermore, by performing dark lock-in thermography, photoluminescence (PL), and scanning electron microscopy studies, we are able to detect various morphological defects in the tandems with poor performance, such as ohmic shunts originating from defects in the bottom CIGSe cell, or from cracking/delaminating of the perovskite top cell. Finally, by correlating the detected shunts in the tandems with PL-probed bottom device, we can conclude that not all defects in the bottom device induce ohmic shunts in the tandems since the NiO_x:Cu + SAM HTL bi-layer can decouple the growth of the top device from the rough, defect-rich and defect-tolerant bottom device and enable high-performing devices.

1. Introduction

As single-junction solar cells are approaching their detailed balance limit of efficiency [1], the photovoltaic research has shifted its focus toward tandem configurations that diminish the thermalization losses in the single-junction solar cells and enable (theoretical) efficiencies of above 40%. Currently, the most popular tandem configurations consist of a low-bandgap ($E_g \sim 1.0 - 1.1$ eV) bottom device such as silicon (Si) or copper–indium–gallium–diselenide (Cu(In,Ga)Se₂, CIGSe) and a top, high-bandgap ($E_g \sim 1.6 - 1.7$ eV) metal-halide perovskite device [2, 3].

Currently, the monolithic Si-perovskite and CIGSe-perovskite tandem solar cells have certified efficiencies of 32.5% [4] and 24.2% [5], respectively. Although the CIGSe-perovskite monolithic tandem solar cells are superior to the Si ones in terms of their tunable and direct bandgap [6], high absorption coefficient that leads to lower material demand and processing costs, and suitability for flexible and facade integrations [7, 8], the common interpretation is that their power-conversion efficiency (PCE) and yield have

been set back by the defect-rich and rough CIGSe cell which then induces shunt-resistance losses, even in the highly-performing monolithic CIGSe-perovskite tandem solar cells [5].

There are two options to address this issue. One is to co-evaporate CI(G)S(e) absorbers with lower surface roughness, as discussed by Ruiz *et al* who achieved a certified efficiency of 23.35% for a monolithic CuInSe₂ (CIS)-perovskite tandem solar cell [9]. However, as any viable top-device technology should not be limited by the morphology of the bottom device as well as because the current industrial standard for the single-junction CIGSe cells is to use rough absorbers [10], a more industrially-attractive approach would be to develop hole-transporting layers (HTLs) which conformally cover the rough bottom-cell surface and enable high shunt resistance and fill factor (FF).

So far, only ALD (atomic layer deposition) nickel oxide (NiO_x) + PTAA (poly[bis(4-phenyl)(2,4,6-trimethylphenyl)amine] [11] and self-assembled monolayers (SAMs) with phosphonic acid as anchoring groups [2, 5] have yielded a PCE higher than 20% on cell areas larger than 0.8 cm². The certified world-record 24.2%-efficient monolithic CIGSe-perovskite solar cell was obtained with Me-4PACz ([4-(3,6-dimethyl-9H-carbazol-9-yl)butyl]phosphonic acid) SAM as an HTL and had a V_{oc} of 1.77 V and a FF of 71.2% [5]. However, its FF was lower than the 76% FF of the tandem with NiO_x + PTAA [11], opening up the question of how we can enable a shunt-free preparation of the top device while insulating possible shunts in the bottom device from the complete device stack.

Motivated by the promising results in the tandem with ALD NiO_x, as well as because of the NiO_x's stability in air [12, 13], suitable opto-electronic properties for solar-cell applications [14], and low-cost deposition [15–19], this paper focuses on its implementation into monolithic CIGSe-perovskite tandems. Instead of using ALD [5], we focus on low-temperature radio frequency (RF) magnetron sputtering of 2% copper-doped NiO_x (NiO_x:Cu) in an effort to avoid the need of the high-temperature post-deposition treatment of the ALD NiO_x which might damage the CIGSe cell [20].

We opt for NiO_x:Cu instead of undoped NiO_x since low-temperature sputtered NiO_x has been shown to induce V_{oc} losses in (single-junction) perovskite solar cells, either due to insufficient selectivity of the NiO_x [21], poor perovskite crystallization [22–24] or redox reactions at the NiO_x-perovskite interface [25]. NiO_x:Cu, however, has been shown to boost the V_{oc} and yield a (non-certified) PCE as high as 20.26% for a 1 cm² single-junction MAPbI₃ solar cell [26]. This is one of the highest reported values for a perovskite device with NiO_x without any chemical surface treatment.

In addition to doping, chemical treatments and passivation of the NiO_x have also been shown to boost the V_{oc} in the perovskite solar cells with either doped or undoped NiO_x as an HTL [5, 9, 27–29]. For the monolithic CIGSe-perovskite tandems, passivating the NiO_x surface with the SAMs is a reasonable choice, since in addition to the SAMs implementation in the current world-record efficiency for the CIGSe-perovskite monolithic tandems [5], they have already also been used in combination with NiO_x to yield highly-efficient monolithic CIGSe-perovskite [9] or Si-perovskite tandems with textured Si [30, 31].

Motivated by the successful results with Cu doping or SAM surface passivation, our work focuses on using NiO_x:Cu with or without SAM surface passivation as an HTL in monolithic CIGSe-perovskite tandem solar cells. We use the MeO-2PACz SAM ([2-(3,6-dimethoxy-9H-carbazol-9-yl)ethyl]phosphonic acid) since the NiO_x + MeO-2PACz HTL bi-layer has already been investigated and shown to yields high and reproducible performance with negligible V_{oc} losses [32].

In addition to investigating the performance of NiO_x:Cu as an HTL in the monolithic CIGSe-perovskite tandems, we are also looking how the bottom device, the processing conditions of the HTL, or the top device can influence the shunt and macroscopic-defects formation in the tandems. Investigating and understanding the shunts in the CIGSe-perovskite tandems is of paramount importance for their further development, specifically with respect to increasing the yield and the reproducibility of the tandems.

Since the CIGSe absorbers are highly defect rich and defect tolerant, it is likely that there are certain defects that do not harm the single-junction CIGSe devices, but possibly shunt the top perovskite device in the tandem configuration. However, as tandems' efficiencies of 23%–24% have been reached by now by using these kind of absorbers in the tandem devices, it is unlikely that *every* defect in the CIGSe device would harm the top device.

Therefore, the understanding whether the rough surface is the only limiting factor for the performance of the monolithic CIGSe-perovskite tandem solar cells is currently lacking. We aim at filling this gap by investigating a variety of chemical and electronic changes as well as macroscopic defects in the tandems and pin-pointing how they affect the FF of the tandem devices. By combining multiple characterization techniques, we are able to show that the processing conditions of the HTL can play a role in the tandems' performance, as well as that the ohmic shunts in the finished tandems can originate either from the bottom or the top device. Therefore, our work disentangles the role of the HTL, the bottom, and the top device on the shunts formation in the complex monolithic stack and as such, presents a step forward in our understanding of the future optimization of the tandems.

2. Results and discussion

We present current density–voltage (JV) measurements in forward-bias and reverse-bias scan direction for tandem solar cells with identically-processed bottom (CIGSe) and top (perovskite) devices, but alterations in the HTL. There are four different HTL configurations used: air- or N_2 -transferred NiO_x :Cu with or without SAM (MeO-2PACz) surface passivation. Two tandems are manufactured with each HTL configuration, resulting in total of eight tandem devices.

The results are structured in the following way. The first two subsections focus on investigating the influence of the current mismatch and of any chemical, electronic, or morphological changes in the HTL due to the air- or the N_2 exposure on the FF. The chemical and electronic changes at the NiO_x :Cu surface are investigated via x-ray and ultraviolet photoelectron spectroscopy (XPS/UPS). The role of the current mismatching on the tandem's FF is investigated by performing JV measurements at varying blue- or red-light intensity. The possible macroscopic defects in the HTL, such as island formation or clustering during the NiO_x :Cu sputtering, are investigated via energy-dispersive x-ray (EDX) spectroscopy. The third subsection focuses on the investigation of the macroscopic defects in the bottom and/or the top device. The finished tandems are imaged with dark lock-in thermography (DLIT) and the DLIT-detected ohmic or non-linear shunts are then correlated to the photoluminescence (PL)-probed bottom and scanning-electron microscope (SEM)-imaged top device.

2.1. Influence of the processing environment of the HTL on the performance of the tandem solar cells

Looking at the solar-cell parameters in table 1 and figure 1, one sees that both devices with N_2 -transferred NiO_x :Cu + SAM are highly-efficient with PCEs in the range of 22%–23% and a FF of 77%–78% on a device area of 1.08 cm^2 . To the best of our knowledge, this is the highest-reported (non-certified) FF in a monolithic CIGSe-perovskite tandem. However, the devices with air-transferred NiO_x :Cu + SAM display pronounced FF losses which severely deteriorate the tandems' performance, while the tandems without SAM display completely shunted behavior.

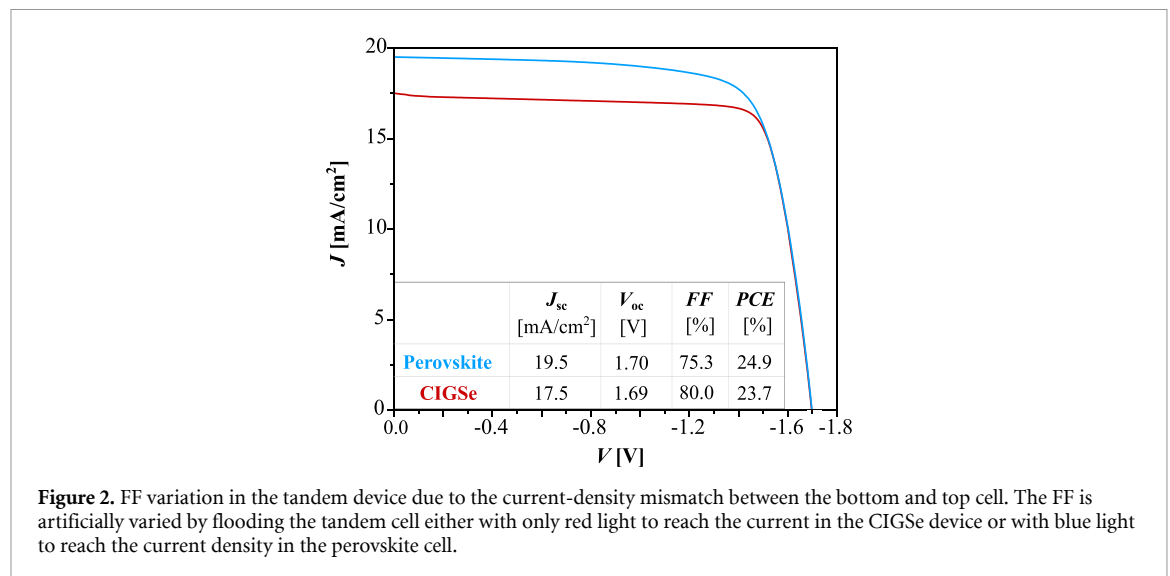
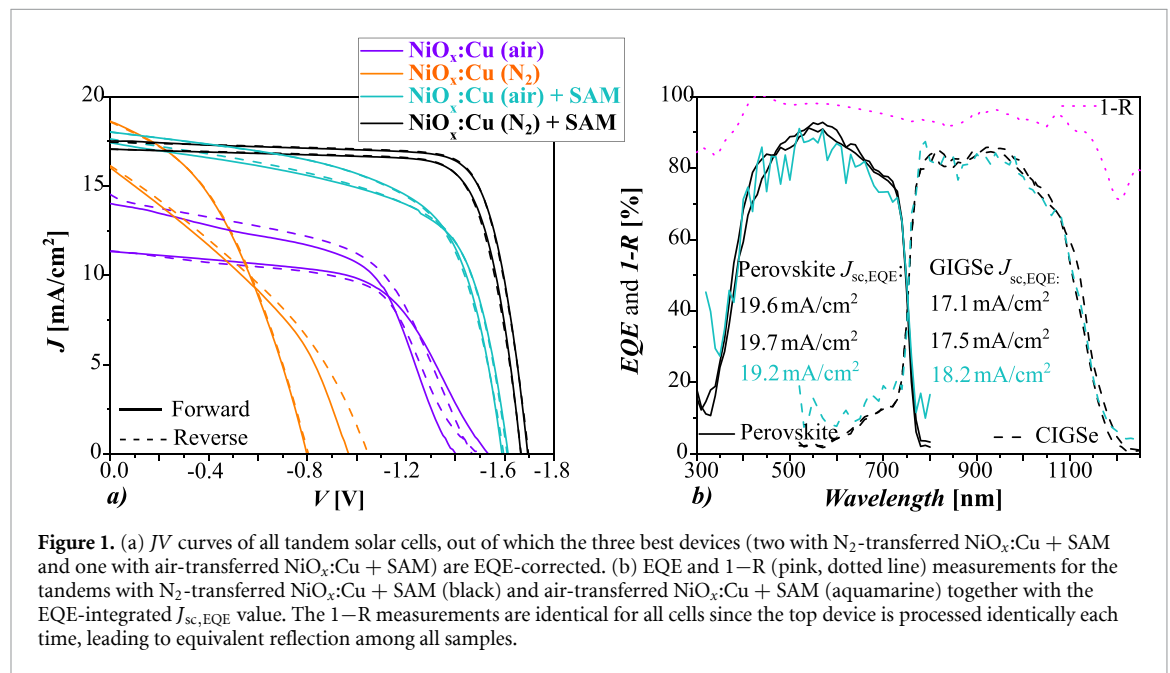
Due to poor FF and shunt resistance of five devices, external quantum efficiency (EQE) was measured only on three NiO_x :Cu + SAM devices: two with the N_2 -transferred NiO_x :Cu (black JV and EQE curves) and one with the air-transferred NiO_x :Cu (aquamarine JV and EQE curves). At a first look, it might seem as if the sample with air-transferred NiO_x :Cu is less current mismatched (19.2 mA cm^{-2} and 18.2 mA cm^{-2} for the perovskite and the CIGSe cell, respectively) than the two samples with N_2 -transferred NiO_x :Cu (19.6 mA cm^{-2} and 17.1 – 17.5 mA cm^{-2} for the perovskite and the CIGSe cell, respectively). However, in the 500–600 nm wavelength region, the EQE signal for the tandem device with air-transferred NiO_x :Cu + SAM indicates around 10% non-negligible absorption, overestimating the EQE-integrated J_{sc} by around 1 mA cm^{-2} . Therefore, all of the tandem devices are almost equally current mismatched, with up to 2.5 mA cm^{-2} difference in the EQE-integrated J_{sc} .

The influence of the current mismatching in two-terminal tandem solar cells on the devices' performance and in particular on the FF has been extensively investigated [33–35]. Various literature sources indicate that operating the tandem device close to or at current-matching conditions results in a FF decrease [33–35]. However, where the minimum FF is reached will greatly depend on the individual performance of both sub-cells. For example, Köhnen *et al* showed that in a monolithic Si-perovskite tandem solar cell, the lowest FF is reached for a slightly limiting Si bottom cell, not at a current-matched cell [36]. Moreover, by combining optical and electrical simulations with devices' data, Köhnen *et al* showed that the FF can vary by almost 1.5% from the lowest FF point (at 0.4 mA cm^{-2} current-density mismatch) to the highest FF point (at around 1.3 mA cm^{-2} current-density mismatch). Therefore, two-terminal solar cells with more pronounced current-density mismatching can often yield an increase in the FF, which somewhat compensates the loss in current density due to the limiting cell.

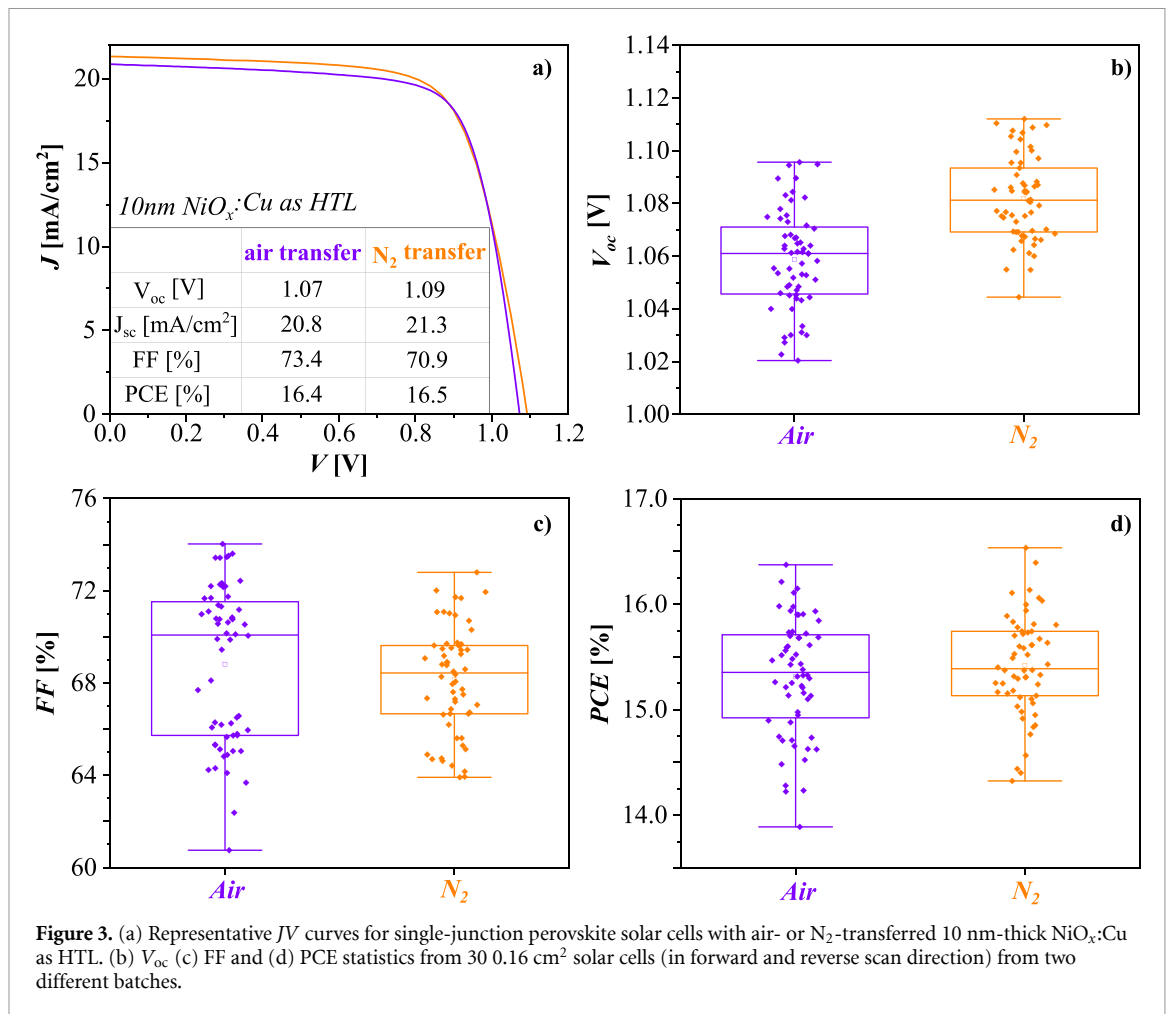
Here a very similar behavior of the FF is detected in the 2.5 mA cm^{-2} current-density mismatched 23.2%-efficient champion device presented in figure 1. In order to test up to which extent the FF obtained in the EQE-corrected JV curve is influenced by this mismatch, either the top cell is artificially flooded with blue, or the bottom cell is flooded with red light. In this way, one can saturate one of the sub-cells in the tandem and limit its current density, offering a deeper insight into the FF and the shunt resistance of each individual sub-cell. As seen in figure 2 below, when the CIGSe's current density of around 17.5 mA cm^{-2} is reached, the FF is increased by around 2% compared to the tandem measured at optimized light spectrum. The high 80% FF of this particular CIGSe cell indicates that the cell's shunt resistance is excellent for tandem applications. On the perovskite side, reaching its current density of around 19.5 mA cm^{-2} yields a FF decrease of around 2.5% compared to the tandem measured at optimized and balanced light spectrum, which then influences the overall tandem's FF.

Table 1. JV parameters of the monolithic CIGSe-perovskite tandem solar cells with air- or N₂-transferred NiO_x:Cu with or without SAM (MeO-2PACz) surface passivation. The J_{sc} values for the last three devices are EQE corrected by using the J_{sc,EQE} values from figure 1(b) below.

HTL Configuration	J _{sc} (mA cm ⁻²)		V _{oc} (V)		FF (%)		PCE (%)	
	Forw.	Rev.	Forw.	Rev.	Forw.	Rev.	Forw.	Rev.
NiO _x :Cu (air)	14.0	14.5	1.40	1.47	54.8	53.2	10.8	11.3
	11.3	11.4	1.53	1.50	57.8	57.9	10.1	9.9
NiO _x :Cu (N ₂)	16.0	16.1	0.97	1.05	35.4	34.1	5.5	5.8
	18.6	18.6	0.80	0.80	40.7	40.9	6.1	6.1
NiO _x :Cu (air) + SAM	17.4	17.6	1.61	1.61	60.7	60.7	17.1	17.2
	18.0	18.0	1.59	1.60	61.4	60.8	17.6	17.5
NiO _x :Cu (N ₂) + SAM	17.1	17.1	1.67	1.67	77.3	77.4	22.0	22.0
	17.5	17.5	1.69	1.69	77.8	78.3	23.1	23.2



Beyond the issue of the current mismatching, the tandem results presented in figure 1 imply that the transfer medium of the NiO_x:Cu (air vs N₂) could possibly play a decisive role for the performance of the tandems. The two cells within each pair of tandem solar cells with identical HTL configuration display comparable performance. However, it is not straight-forward to immediately conclude that the transfer



environment of the NiO_x:Cu is the only factor that limits the performance of the tandems, since they are processed via many steps, each one with the possibility to shunt or partially damage the overall tandem in an independent manner from the transfer medium.

In order to exclude all of the uncertainties that are brought in by the CIGSe bottom cell and its rough surface, as well as by the complex tandems' manufacturing, 30 single-junction perovskite small-area (0.16 cm²) solar cells with 10 nm NiO_x:Cu, transferred either via air or N₂ are also manufactured. Figure 3 presents the champion JV curves with respect to the PCE, as well as statistics on the devices' V_{oc}, FF and PCE. The tabulated statistical distribution of the JV parameters alongside all 30 JV curves can be found in the supplementary information.

Compared to the N₂-exposed NiO_x:Cu, the air-exposed NiO_x:Cu in the single-junction perovskite solar cells exhibits an average 20 mV decrease in the V_{oc} and more pronounced fluctuations in the FF. In some of the batches, the FF is in the range of 70%–74%, while in others in the range of 64%–66%. The FF for the N₂-transferred NiO_x:Cu is lower in its record values, but it is statistically more reproducible, with values often in the range of 67%–70%. Finally, the PCE does not suffer too much by the air exposure of the NiO_x:Cu, because the loss in V_{oc} is often compensated by a gain in the FF.

The single-junction results offer several important insights into the influence of the NiO_x:Cu's air exposure on the NiO_x:Cu-perovskite interface. Firstly, the reproducibility of the devices with air-transferred NiO_x:Cu is more challenging, very likely because of variations in exposure length and air humidity across batches. Secondly, a statistically-relevant loss in the V_{oc} is detected, but this effect is not as pronounced in the single-junction solar cells as it is in the tandems.

In order to look into some possible causes for the different reproducibility and the V_{oc} losses, XPS and UPS measurements are performed and the surface chemistry and electronics of the NiO_x:Cu right after sputtering without breaking the vacuum, or exposed short-term (1 h) or long-term (24 h) to either air or nitrogen are investigated. Via XPS, the Ni 2p, O 1s, C 1s, and Cu 2p core peaks in the NiO_x:Cu films deposited either on CIGSe cells (tandem configuration) or **indium tin oxide (ITO)** (single-junction configuration) are measured.

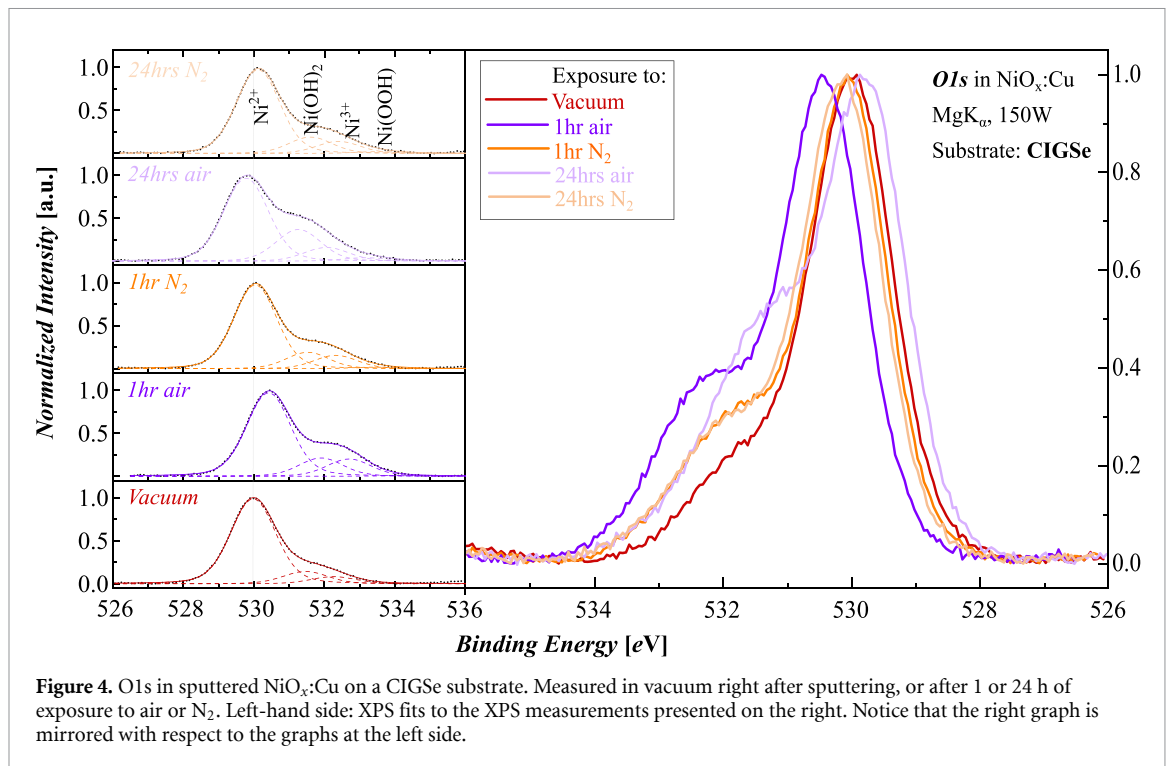


Figure 4. O 1s in sputtered $\text{NiO}_x\text{:Cu}$ on a CIGSe substrate. Measured in vacuum right after sputtering, or after 1 or 24 h of exposure to air or N_2 . Left-hand side: XPS fits to the XPS measurements presented on the right. Notice that the right graph is mirrored with respect to the graphs at the left side.

NiO_x and all of its doped variations have two co-existing oxidation states: NiO (Ni^{2+}) and Ni_2O_3 (Ni^{3+}) [14, 16]. The most common defect in NiO_x is the Ni^{2+} interstitial vacancy ($\text{V}_{\text{Ni}^{2+}}$), which is compensated for by the Ni^{3+} species [14]. Many groups investigate the XPS core peak of Ni 2p and decompose it into the two above-mentioned oxidation states [14, 16, 25, 37, 38] and additionally either $\text{Ni}(\text{OH})_2$ or $\text{Ni}(\text{OOH})$, or both, due to air contamination, while others wrongly assign the dominant peak as NiO contribution only and the remaining part as a $\text{Ni}(\text{OOH})$ contribution [20].

Assigning three to four peaks to the Ni 2p core peak, out of which two clearly distinguish between Ni^{2+} and Ni^{3+} , is in principle correct, but the extracted contributions from the fits cannot be considered as absolute values because NiO_x exhibits multiplets splitting [39]. The multiplets splitting requires each of the three to four sub-peaks (Ni^{2+} , Ni^{3+} , $\text{Ni}(\text{OH})_2$, and/or $\text{Ni}(\text{OOH})$) in the Ni 2p core peak to be further de-convoluted in three to four multiplets per sub-peak. Such a sophisticated deconvolution of the Ni 2p peak is often not attainable via a state-of-the-art XPS fitting software, primarily because the Ni 2p peak is limited by the XPS set-up in its intensity and signal-to-noise ratio, making its deconvolution and the detection of sometimes subtle changes even more challenging.

Another approach is to fit the O 1s with the respective four contributions (O 1s NiO, Ni_2O_3 , $\text{Ni}(\text{OH})_2$, and/or $\text{Ni}(\text{OOH})$). In this work, the air-free transfer of the $\text{NiO}_x\text{:Cu}$ from the sputter to the XPS/UPS analytic chamber enables us to obtain a reference for the XPS fitting procedure of the O 1s peak since all external contamination for these measurements is eliminated (or, at least kept as a systematic error). We can then compare the trend in the evolution of the O 1s peak as the $\text{NiO}_x\text{:Cu}$ films are exposed to air or nitrogen.

The O 1s peaks from the CIGSe + $\text{NiO}_x\text{:Cu}$ measurements and their fits are presented in figure 4, while the extracted contribution from the fits for each species in the $\text{NiO}_x\text{:Cu}$ are presented in table 2. The remaining XPS measurements on the $\text{NiO}_x\text{:Cu}$ deposited on a CIGSe cell and all of the measurements on ITO can be found in the supplementary information.

For the as-deposited $\text{NiO}_x\text{:Cu}$ (measured right after sputtering, without breaking vacuum), the dominating oxygen contribution (O in NiO, or Ni^{2+} oxidation state of the NiO_x) is found around 530 eV binding energy regardless if the $\text{NiO}_x\text{:Cu}$ is deposited on CIGSe or ITO. The Ni^{2+} , $\text{Ni}(\text{OH})_2$, Ni^{3+} , and $\text{Ni}(\text{OOH})$ contributions in the as-deposited $\text{NiO}_x\text{:Cu}$ films are also independent of the substrate. The one-hour N_2 -exposed films show non-significant $\sim 2\%$ – 3% difference in the amount of $\text{Ni}(\text{OH})_2$ and Ni^{3+} amount with respect to the change of substrate, meaning that the $\text{NiO}_x\text{:Cu}$ surface chemistry is stable and reproducible post-sputtering and after short N_2 exposure.

The 24 h N_2 exposure and both the 1 h and 24 h air exposure result in different surface chemistry with respect to the substrate. However, as the surface chemistry of the as-deposited $\text{NiO}_x\text{:Cu}$ is identical for both of the substrates, these changes are not likely to be induced by the substrate, but rather by the varying

Table 2. XPS fit of the O1s core peak in NiO_x:Cu sputtered on a CIGSe cell or on an ITO substrate. The error of the measurements, which is in the range of 0.1–0.5 eV and stems from the fitting procedure, is removed from the table due to simplicity.

Exposure	Ni ²⁺ (%)		Ni(OH) ₂ (%)		Ni ³⁺ (%)		Ni(OOH) (%)	
	CIGSe	ITO	CIGSe	ITO	CIGSe	ITO	CIGSe	ITO
As-deposited	81.5	80.8	11.7	12.0	6.8	7.2	0	0
1 h N ₂	73.0	73.8	14.2	16.9	11.6	7.9	1.3	1.4
24 h N ₂	73.7	69.6	14.3	20.3	10.5	6.9	1.5	3.3
1 h air	70.0	64.8	15.3	25.6	14.4	7.1	0.3	2.5
24 h air	63.1	59.8	24.0	26.5	10.4	8.9	2.6	4.9

external conditions during the measurements. These results already imply that the air exposure can induce changes in the surface chemistry from one batch to another, depending on the air temperature and humidity. This effect is less pronounced for the 24 h N₂-exposed NiO_x:Cu because the N₂ environment has significantly lower humidity.

With respect to the changes in the surface chemistry post-exposure, N₂-exposed NiO_x:Cu deposited either on the CIGSe cell or on the ITO substrate exhibits around 7%–8% decrease in the Ni²⁺ amount, and a 3%–5% and 1% increase in the Ni(OH)₂ and Ni(OOH) species, respectively compared to the as-deposited NiO_x:Cu. After the initial changes in the first hour, the surface chemistry of the N₂-exposed NiO_x:Cu stabilizes for the CIGSe substrate, but changes slightly for the ITO substrate, as demonstrated by the 4% decrease in the Ni²⁺ and a ~2%–3% increase in the Ni(OH)₂ and Ni(OOH) amount.

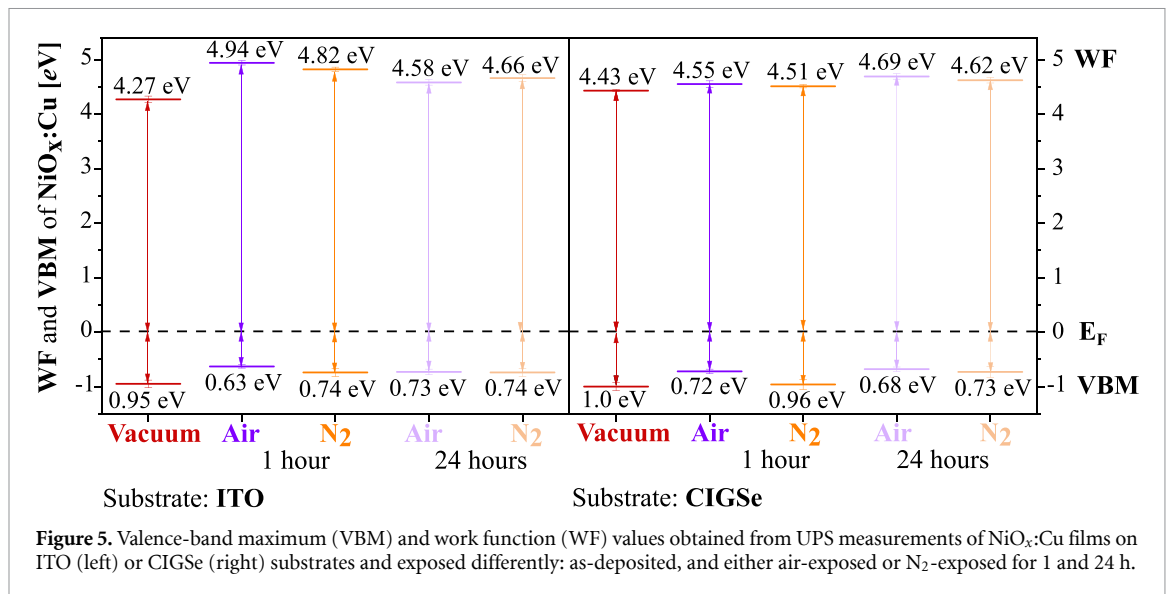
The air exposure results in a prominent loss in the Ni²⁺ contribution. Compared to the as-deposited NiO_x:Cu, the one-hour air exposure results in ~12% and 16% loss in the Ni²⁺ contribution for the CIGSe and the ITO substrate, respectively. After a 24 h exposure, a decrease of around 20% in the Ni²⁺ species is detected independently of the substrate, accompanied with a prominent 12%–14% increase in the Ni(OH)₂ species due to continuous adsorption of water on the NiO_x:Cu surface. This effect could be influencing the NiO_x:Cu-perovskite interface in a two-fold manner.

Firstly, since the perovskite crystal is prone to humidity-induced degradation, a high amount of hydroxide species at the NiO_x:Cu-perovskite interface will worsen the wetting of the perovskite precursor solution, decrease the carrier concentration, increase the resistivity and decrease the hole mobility, eventually leading to V_{oc} and FF losses [20]. For ALD NiO_x, this issue has been overcome by performing a high-temperature (300 °C) post-deposition treatment. However, similar to the results presented in [11], we are avoiding an annealing post-treatment of the NiO_x:Cu since the 180 °C–200 °C temperature that the CIGSe can be exposed to without risking Cd-diffusion into the CIGSe absorber from the CdS layer is not high enough to decrease the hydroxides content.

Secondly, opposed to high-temperature annealed NiO_x or NiO_x:Cu, low-temperature deposited NiO_x(:Cu) suffers from worse crystallinity and higher concentration of surface states, defects, and impurities [40]. At low-temperature processing, the number of Ni²⁺ vacancy defects is higher since the NiOOH species are not eliminated via the usual high-temperature annealing post-deposition treatments. Literature has already pin-pointed that a higher Ni³⁺ amount can also cause a loss in the conductivity, unfavorable accumulation of holes at the NiO_x-perovskite interface, high rate of trap-assisted interfacial recombination, reduced collection and extraction of holes, and last, but not least, accelerated degradation [41]. Additionally, it has been shown that a higher amount of Ni³⁺ species for *sputtered* NiO_x leads to an elevated amount of interfacial redox reactions and increased formation of PbI_{2-x}Br_x-rich phases [42]. Consequently, as the XPS measurements reveal loss in the Ni²⁺ amount during the air exposure, one can expect a degradation of the NiO_x:Cu interface, inducing V_{oc} losses.

The UPS measurements presented in figure 5 investigate how the air and N₂ exposures influence the work function (WF) and valence-band maximum (VBM) of the NiO_x:Cu deposited either on ITO (corresponding to single-junctions configuration) or deposited on CIGSe (corresponding to tandem configuration).

Comparing the NiO_x:Cu deposited on ITO (LHS of figure 5) to the one deposited on CIGSe (RHS of figure 5), the most striking difference is seen in the WF. The short air- or N₂-exposure of the NiO_x:Cu deposited on CIGSe leads only to around 0.1 eV increase from the WF measured in vacuum, unlike the 0.55–0.67 eV WF increase detected for the NiO_x:Cu deposited on ITO. This results in a 0.3–0.4 eV smaller WF of the NiO_x:Cu deposited on CIGSe compared to the NiO_x:Cu deposited on ITO. As the air and N₂ exposure is prolonged to 24 h, the WF of the NiO_x:Cu deposited on ITO decreases, while on CIGSe it increases—changes which eventually yield almost equal WF (4.58–4.69 eV) across all four samples (24 h air- or N₂-exposed NiO_x:Cu deposited either on ITO or CIGSe).



Regarding the VBM, all values differ by no more than 0.1 eV and are in the range of 0.63–0.74 eV, except for the one-hour, N₂-exposed NiO_x:Cu deposited on CIGSe. With a value of 0.96 eV, the VBM of this sample is very close to the VBM measured in vacuum (0.95–1.0 eV).

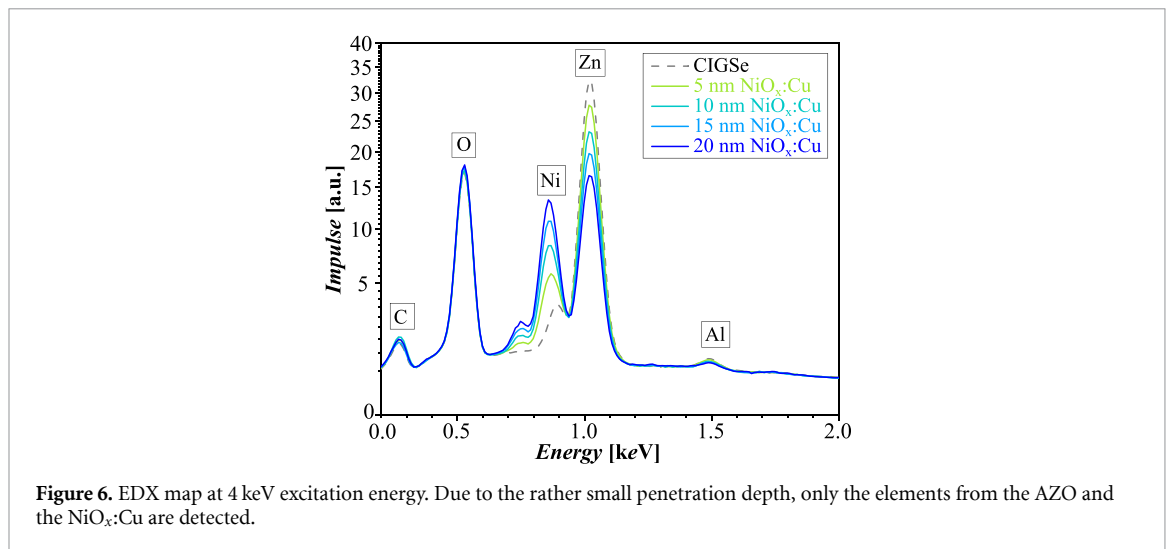
These UPS measurements offer an additional insight as to why the NiO_x:Cu is more poorly performing in the tandem devices as a stand-alone HTL as well as why the short air or N₂ exposure does not influence the single-junction solar cells very prominently. The low WF of the NiO_x:Cu deposited on CIGSe will lead to unfavorable band alignment—regardless if the samples are exposed to air or N₂. This is not the case for the NiO_x:Cu deposited on ITO, where the WF of the air-exposed NiO_x:Cu is even larger than the N₂-exposed NiO_x:Cu. Combining the low WF and the unfavorable VBM, with the increase in the hydroxides and decrease in the Ni²⁺ amount for the air-exposed NiO_x:Cu, it can be concluded that the detected changes in the surface chemistry could (partially) explain why the air exposure of the NiO_x:Cu is not beneficial for the tandem solar cells.

Going a step further and considering the SAM surface passivation, it has been demonstrated that SAMs can induce dipole moments on the surface of metal oxides (MOs) and change their WF [43, 44]; passivate the MO's oxygen vacancies or perovskite defects via chemical bonding [45–47]; affect the growth of the perovskite crystal [48]; or, speed up the holes extraction at the MO-perovskite interface [49]. Therefore, it is very likely that the MeO-2PACz simultaneously passivates the Ni²⁺ vacancies and improves the band alignment at the NiO_x:Cu-perovskite interface, explaining why the NiO_x:Cu + SAM HTL bi-layer leads to more-efficient tandems than NiO_x:Cu as a stand-alone HTL. Finally, the effect of the SAM surface passivation is more prominent with the N₂-transferred NiO_x:Cu due to its higher Ni²⁺ amount compared to the air-transferred NiO_x:Cu.

However, it is still questionable up to which extent these changes in the NiO_x:Cu surface chemistry (could) induce V_{oc} and FF losses in the (tandem) solar cells and whether it can be concluded that the varying surface chemistry is the only culprit for the varying performance of the tandems. Firstly, if air-induced changes in the NiO_x:Cu surface chemistry are the only reason for the worsened performance of the tandems, why are then the tandems with N₂-transferred NiO_x:Cu more severely shunted than the tandems with the air-transferred NiO_x:Cu? Secondly, what is the influence of the underlying CIGSe cell on the top device and can certain PCE-limiting defects develop in the tandems, independent of the transfer medium for the NiO_x:Cu?

These questions open up the investigation of several hypotheses that go beyond the transfer medium of the HTL and that each could explain the primary causes for the observed shunting. One possible explanation is that a non-conformal coverage of the surface of the CIGSe bottom device stack due to too thin, 10 nm NiO_x:Cu would induce shunts in the tandems in the absence of the SAM. Another possible explanation is that either numerous defects, varying morphology, and/or shunts either in the bottom or in the top cell would create ohmic shunts in the whole tandems, thereby completely sabotaging its performance.

In order to test these hypotheses, we perform (1) EDX spectroscopy measurements of NiO_x:Cu deposited on a CIGSe cell to investigate the coverage of the CIGSe cell; (2) DLIT and PL imaging of the tandems to investigate if there are any ohmic shunts in any of the devices; and (3) SEM top-view imaging of the tandems



to investigate if there are any defects, such as cracks, in the perovskite film that might limit the tandems' performance.

2.2. EDX mapping of NiO_x:Cu sputtered on a CIGSe cell

The EDX mapping is performed on 5 nm, 10 nm, 15 nm and 20 nm thick NiO_x:Cu deposited on CIGSe in order to investigate whether holes or island growth are present for any of these thicknesses. Two excitation energies are used: 15 keV and 4 keV. The 15 keV excitation energy has a larger penetration depth into the material, but the signal-to-noise ratio is lower compared to the measurements at 4 keV. Therefore, the following discussion is centered around the results obtained with 4 keV excitation energy, which yields higher surface sensitivity and maps the surface morphology. The results with 15 keV excitation energy can be found in the supplementary information.

With a 4 keV excitation energy, many of the elements within the CIGSe bulk are not detected. Instead, as seen in figure 6, only the NiO_x:Cu, the underlying aluminum-doped zinc oxide (AZO), and the surface contamination are detected. The Cu is detected with the 15 keV excitation energy and its increase alongside with the increasing NiO_x:Cu thickness (supplementary information). One downside of mapping with 4 keV excitation energy is that the Ni *L*_α line overlaps with the *L*_α line of Zn. However, by measuring a bare CIGSe reference, one can clearly see the initial Zn signal (dashed line in figure 6) and then its step-wise suppression as progressively thicker NiO_x:Cu films are measured. The larger NiO_x:Cu content is additionally confirmed by the hand-in-hand increasing Ni signal with the increasing thickness.

The elemental map in figure 7 below shows that Ni is present across the full CIGSe surface for all thicknesses. However, accompanying top-view SEM of the samples with 10 nm- and 20 nm-thick NiO_x:Cu reveals dark spots in parts of the sample (red-circled areas in figures 7(b) and (d)). To investigate the origin of these dark patches, we performed a full EDX elemental mapping for the 10 nm-thick NiO_x:Cu.

As seen in figure 8, the darkened areas in the SEM images correlate to an increase in the carbon content in the EDX map. This indicates that the NiO_x:Cu is not forming islands or leaving parts of the AZO uncovered, but that instead on two of the samples (10 nm and 20 nm NiO_x:Cu) there is a larger amount of dirt, possibly glove residues, or other organic residues (for example, due to cleaning of the AZO). This hypothesis is also confirmed by the suppression of the signals of the other elements at the most-bright carbon patch. In conclusion, the EDX mapping shows no evidence of holes, island growth, or improper coverage of the AZO by the sputtered NiO_x:Cu. Therefore, a 10 nm-thick NiO_x:Cu should be sufficiently thick for the tandem devices. The shunting in the tandems with N₂-transferred NiO_x as a stand-alone HTL is concluded to originate elsewhere.

2.3. Shunt investigation in the tandem solar cells via DLIT and PL imaging

We now investigate the presence of shunts in the finished tandem devices via DLIT and PL imaging. The DLIT measurements enable a distinction between non-linear and ohmic shunts to be made, while PL or the later-presented SEM imaging can aid us in understanding whether the shunts originate in the CIGSe or perovskite solar cell.

The DLIT measurements of the solar cells are performed by applying a pulsed voltage in the dark, either at high-injection (*I*_{sc} of the solar cell) or at low-injection mode at forward or reverse bias [50]. If the dark

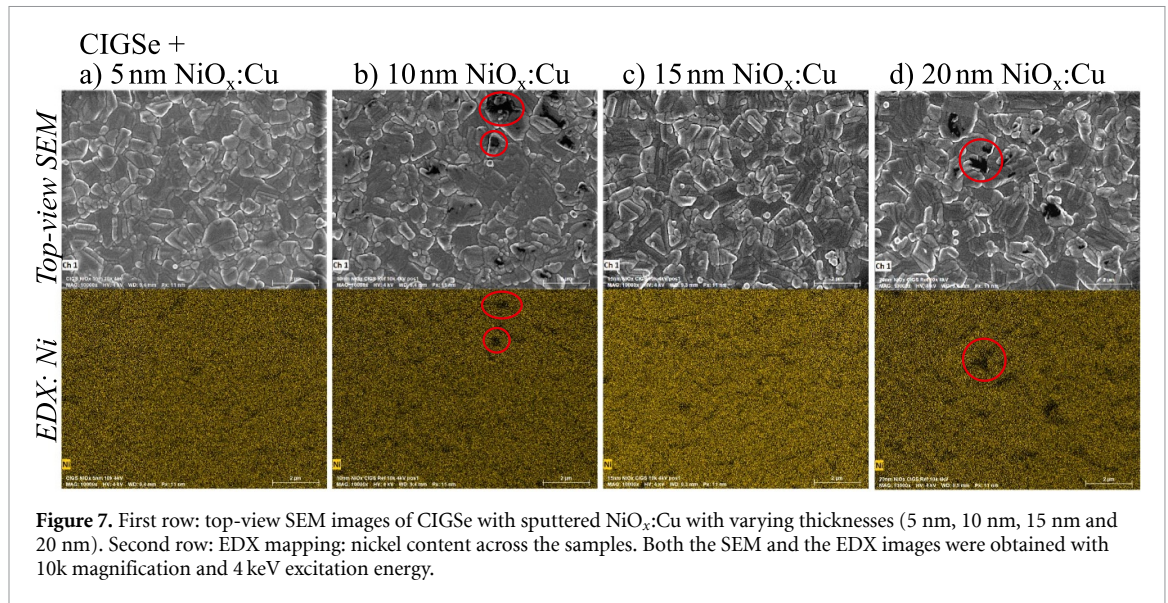


Figure 7. First row: top-view SEM images of CIGSe with sputtered NiO_x:Cu with varying thicknesses (5 nm, 10 nm, 15 nm and 20 nm). Second row: EDX mapping: nickel content across the samples. Both the SEM and the EDX images were obtained with 10k magnification and 4 keV excitation energy.

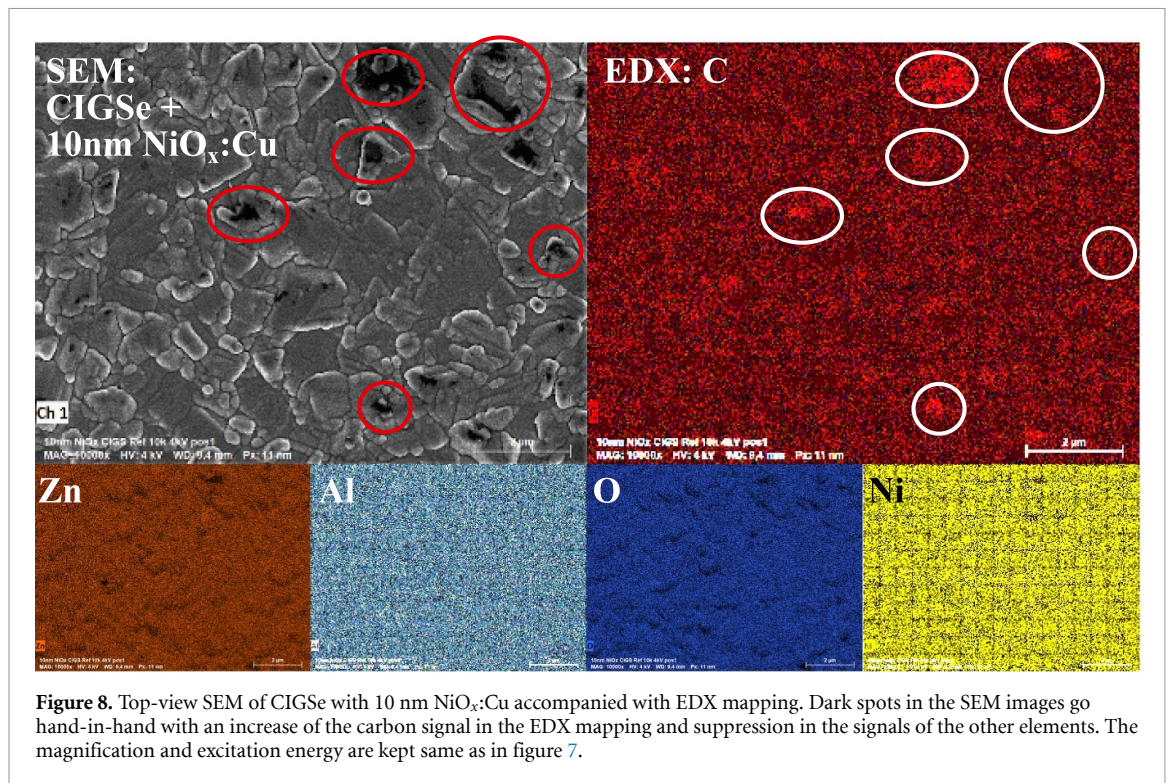


Figure 8. Top-view SEM of CIGSe with 10 nm NiO_x:Cu accompanied with EDX mapping. Dark spots in the SEM images go hand-in-hand with an increase of the carbon signal in the EDX mapping and suppression in the signals of the other elements. The magnification and excitation energy are kept same as in figure 7.

current that flows through the cell encounters a shunt site, the current increases and yields hot spots which are then displayed in the DLIT image.

The detected hot spots are result of heat dissipation which may be generated via several mechanisms in the cell. The most common and simplest case is when a current flows through a conductor with a significant ohmic resistance and radiates heat (also known as Joule heat) [51]. Understanding the nature of the hot spots and their behavior under different biasing conditions enables a distinction between linear (ohmic) and nonlinear shunts to be made [50]. This is achieved by collecting DLIT images both at high and low injection and in forward and reverse bias. If the hot spot is displayed in all of the images, then the shunt is ohmic. If the hot spot disappears in the low-injection, reverse-bias mode, then the shunt is non-linear [50].

The DLIT measurements yield two types of images: an amplitude image A and a phase image Φ at two different frequencies and at different times (for more details refer to the experimental section). The amplitude image presents the magnitude of the current that flows through a shunt and accordingly displays brighter or darker spots depending on the shunt strength [50]. The phase image displays all shunts regardless

of their strength and by scaling in degrees, it gives information about a phase shift between the measured and the reference signal [50].

The DLIT images indicate that each pair of tandems with identical HTL configuration (air- or N_2 -transferred $NiO_x:Cu$ with or without SAM) exhibits very similar distribution of shunts and heat dissipation. Additionally, the (lack of) defects that are detected in the DLIT images go hand-in-hand with the changes in the performance of the devices as the HTL configuration is changed. Figure 9 presents four DLIT and PL images—one for each HTL configuration—while the remaining images for the other four tandem devices can be found in the supplementary information.

2.3.1. Ten nanometer $NiO_x:Cu$ as a stand-alone HTL, N_2 transfer

The DLIT images of the worst-performing devices with $NiO_x:Cu$ as a stand-alone HTL transferred through N_2 presented in figure 9(A) indicate the presence of many ohmic and non-linear shunts which completely sabotage the performance of the tandems. PL imaging at 650 nm with InGaAs laser diode (figure 9(A-e)) was also performed in order to obtain solely a signal from the underlying CIGSe cell. Five prominent bright spots are detected in the PL signal, on the exact same location as the shunts detected in the DLIT measurements. Looking at the high- and low-injection regimes for the DLIT measurements, one also notices that these spots do not disappear completely in the reverse, low-injection mode, confirming the presence of ohmic shunts. The combination of the PL and DLIT measurements implies that most likely the ohmic shunts in the tandem are caused by the bottom CIGSe device, explaining why the N_2 -transferred $NiO_x:Cu$ as a stand-alone HTL is the worst-performing HTL configuration.

However, the bright PL spots do not have to mean that the underlying CIGSe absorber or the bottom cell has been shunted to start with. While a shunted CIGSe absorber/device is a possibility, an additional explanation could also be that the CIGSe device has had a number of defects that would not have harmed the FF of a single-junction CIGSe device, but that these defects—at some point along the manufacturing process chain—would induce ohmic shunts in the tandems. However, without PL images and *JV* measurements on the bottom device prior to its implementation in the tandems, distinguishing between these two hypothesis is not straight-forward.

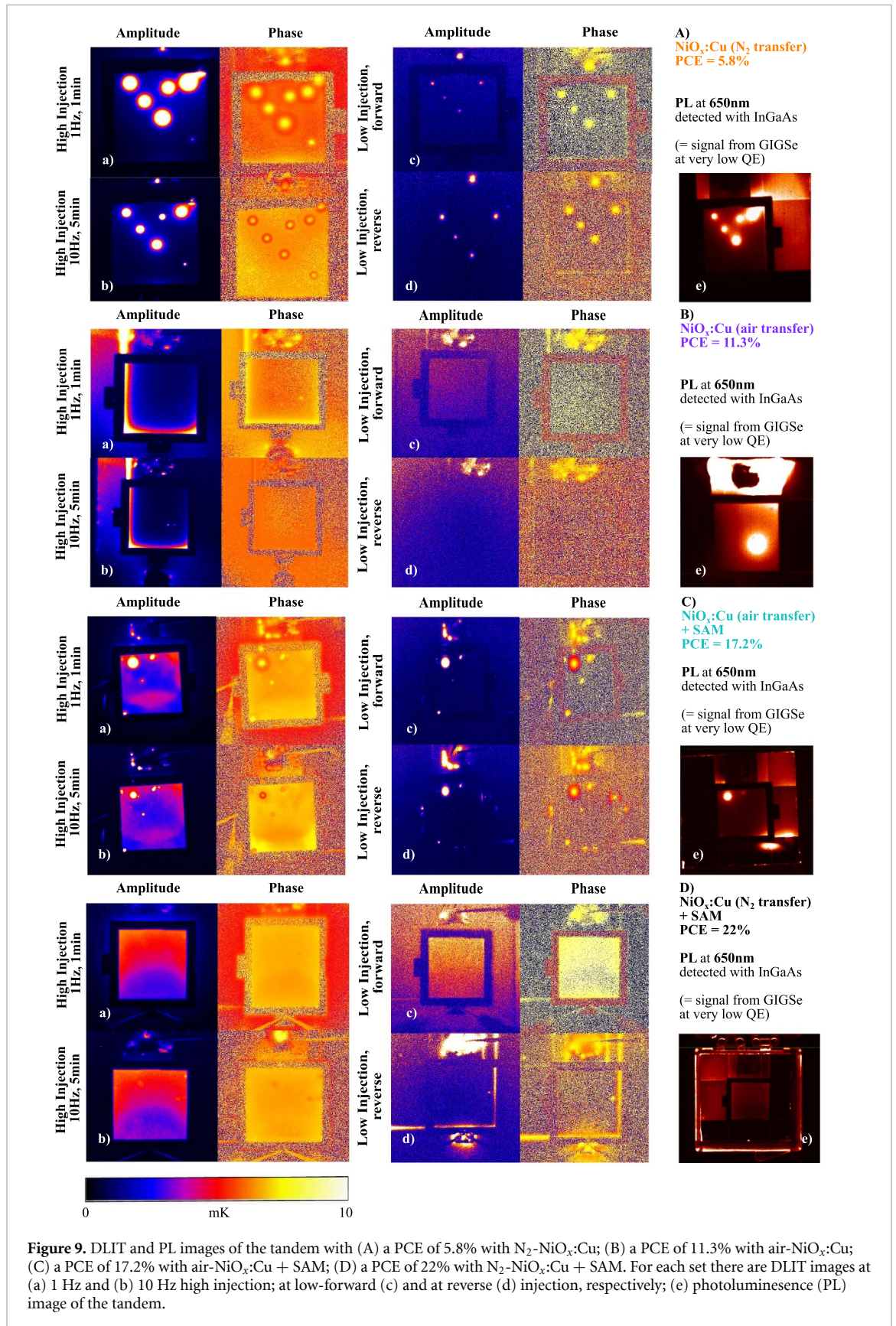
If the bottom cell has been indeed shunted, then it could have gotten shunted prior, during, or after the $NiO_x:Cu$ sputtering; or, the N_2 exposure could have somehow caused the shunting. The last option does not seem very likely since if the N_2 -transfer of the $NiO_x:Cu$ would have been causing such severe shunts in the CIGSe cell, then one would have expected an identical effect on the N_2 -transferred $NiO_x:Cu$ that would later be subjected to SAM spin-coating. The high efficiency of the devices with N_2 -transferred $NiO_x:Cu$ + SAM would then imply that the SAM can somehow ‘heal’ the shunts in the CIGSe cell, which is not realistic. The same argument can be used to exclude shunt formation during the $NiO_x:Cu$ sputtering. Therefore, the tandem shunt-inducing structures in the CIGSe were most likely formed during the CIGSe manufacturing or the handling between individual manufacturing steps. Therefore, whether these shunts are created would vary from sample to sample, thereby limiting the yield and the reproducibility of the devices.

2.3.2. Ten nanometer $NiO_x:Cu$ as a stand-alone HTL, air transfer

The cells with $NiO_x:Cu$ as a stand-alone HTL transferred through air (figure 9(B)) display a few nonlinear shunts at high injection, which, unlike an ohmic shunt, disappear in the low-injection regime. These nonlinear shunts are detected as bright spots on the active area. Additionally, both of the cells with $NiO_x:Cu$ transferred through air (see supplementary information) face an issue of inhomogeneous heat dissipation: one at the contact, while the other within the active area, best visible at high (10 Hz) and long (5 min) injection.

This inhomogeneous heat dissipation is often caused either by non-linear shunts (which would appear as bright spots in all of the images, except in low, reverse injection), by areas with increased recombination currents [52], or by pronounced increase in the tandem’s series resistance caused by Joule heating [53]. Thus, in the absence of both non-linear and ohmic shunts, the cell presented in figure 9(B) could display an increase in the recombination current near the silver ring which then causes the inhomogeneous heat dissipation, in a very similar manner to the recombination currents around bus bars in a Si cell [52]. This inhomogeneous heat dissipation around the silver ring combined with the effect of the air on the $NiO_x:Cu$ surface chemistry explain why these tandems achieved a PCE of only $\sim 11\%$ – 12% .

Additionally, it should be noted that unlike the tandems with N_2 -exposed $NiO_x:Cu$ which were manufactured on a CIGSe cell that induced ohmic shunts in the tandem device (figure 9(A)), the bright spot in the PL image of the tandems with air-transferred $NiO_x:Cu$ (figure 9(B)) indicate that the observed defect in the CIGSe cell has not induced ohmic shunts in the tandems, confirming that not all PL-detected defects in the CIGSe device are limiting the tandem performance.



2.3.3. Ten nanometer $\text{NiO}_x:\text{Cu}$, air or N_2 transfer + SAM

The tandems with air-transferred $\text{NiO}_x:\text{Cu}$ and SAM (figure 9(C)) have one ohmic shunt, accompanied with inhomogeneous heat dissipation around the silver ring and around/from the non-linear shunts. The ohmic shunt is in the same location as the brighter spot in the PL measurement, which could mean that the shunt could originate from the CIGSe cell. However, as we will discuss later, in this case it mostly originates from

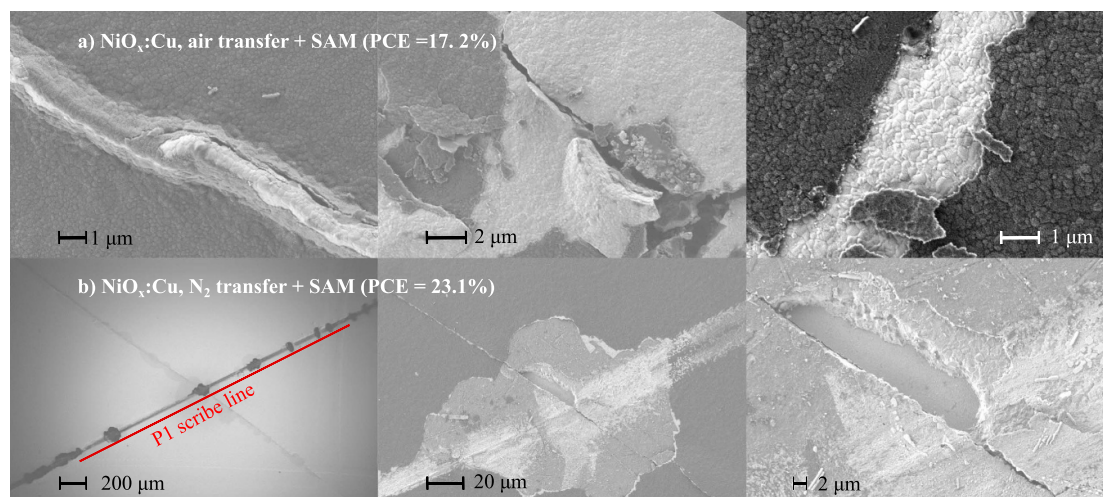


Figure 10. SEM imaging. (a) Various macroscopic morphological defects: cracking, peeling or lift-off of the perovskite at or around large wrinkles on the tandem with air-transferred $\text{NiO}_x\text{:Cu}$ with SAM. (b) Cracking of the perovskite around the P1 scribe on the tandem with N_2 -transferred $\text{NiO}_x\text{:Cu}$ with SAM. The image progressively zooms in from left to right.

the top device because top-view SEM images of the tandems reveal cracked perovskite (figure 10(a)), which is not the case for the devices with ohmic shunts shown in figure 9(A).

The devices with N_2 -transferred $\text{NiO}_x\text{:Cu}$ with SAM (figure 9(D)) show no severe shunts in either the DLIT or the PL images. The 22%-efficient tandem has inhomogeneous heat dissipation, but it is not localized around possible centers of recombination and/or non-linear shunts as for the devices with air-transferred $\text{Ni}_x\text{:Cu}$ (+SAM). The PL image indicates that the device is free of ohmic shunts or defects in the CIGSe cell. The 23%-efficient champion device has a few nonlinear shunts (see supplementary information) that cause a partial inhomogeneous heat distribution. However, unless combined with ohmic shunts or poor CIGSe quality, these non-linear shunts are not problematic. Making the comparison between the air- or N_2 -transferred $\text{NiO}_x\text{:Cu}$ with SAM, one sees that the presence of even one ohmic shunt in the finished tandem can cause absolute losses of around 16% in the FF and 100 mV in the V_{oc} .

2.4. Mechanical defect analysis of the perovskite films via top-view SEM imaging of the tandem solar cells

An important aspect for the improvement of the reproducibility/yield of the tandem devices is to also understand which (mechanical) defects can appear in the top cell and whether they can be limiting for the tandems' performance. Therefore, a selection of top-view SEM images gathered at 2.00 kV accelerating voltage and varying magnifications are used to discuss a multitude of structures on the tandem solar cells. With the exception of figure 10 below, most of the SEM images can be found in the supplementary information.

The most common structure that appears on all of the samples, regardless of the HTL configuration, is dust/surface contamination. Most of the dust particles are not very likely to have been present during the processing of the perovskite film since they show in the SEM images as loosely-attached particles on the surface with a size of up to several microns. However, some dust particles (or contaminants of another form), have adhered on the samples prior to the perovskite deposition, influencing the crystallization of the top device. The SEM images show larger or smaller perovskite crystal sizes on top or away from the contamination, respectively. While it is unlikely that varying perovskite crystal sizes across the cell's active area can fully destroy the tandems, grain boundaries and varying crystallinity of the perovskite absorber can affect the solar-cell performance [23, 54].

Other macroscopic defects—commonly caused by the handling of the tandem devices—present themselves as clusters of many small dots, cracking due to applying pressure with the tweezers, or shallow and foggy lines similar to brush strokes. When outside of the active area, these defects are usually not detrimental for the device performance. This is confirmed also by the fact that smudges and handling defects are detected even on the high-performing devices. However, within the active area, they pose a risk of mechanical scratching of the surface, which would then shunt the whole tandem.

On some samples we also detect black patches, which look like splashed liquid or a smudged layer, and are very likely organic residues anchoring to the tandem's surface, as seen from a closer perspective on the 5.8%-efficient tandem with N_2 -transferred $\text{NiO}_x\text{:Cu}$. In addition, on this sample a grain with a size of several microns was also imaged. The prominent cubic structure of the grain, hints that the defect could be

cesium-related, due to the CsI incorporation in the precursor solution. Such a grain could be a consequence of undissolved cesium particles, or even some cesium-rich perovskite phase. This grain is seen only on one of the worst-performing tandems (figure 9(A)) which already displayed a multitude of ohmic shunts possibly caused by the underlying CIGSe device. But, if found on the active area, this Cs-rich grain could have possibly enhanced the ohmic shunting in the tandem.

Another commonly-detected structure is the wrinkling of the perovskite film, commonly forming when the perovskite precursor solution is exposed to the antisolvent, causing stress in the perovskite film [55]. The choice of the anti-solvent, the concentration of the precursor solution, the type of the perovskite, or the substrate morphology all influence how many and how large wrinkles are formed. The wrinkling often happens around the sample's edges, where the stress of the perovskite film is the largest; around some other defects, such as particles or de-wetted surfaces in the film; or, around uneven structures on the underlying surface, as commonly seen for the rough CIGSe surface.

The wrinkling of the perovskite films is predominantly harmless for the devices, but in some rare cases, it can lead to high stress, breaking off of the perovskite film. This behavior is detected for the 17.2%-efficient device with air-transferred $\text{NiO}_x\text{:Cu}$ with SAM on top of it (figure 10). The breaking, cracking, flaking or peeling off of the perovskite in the cell's active area could have induced the ohmic shunts detected in figure 9(C), since it would have provided a direct contact among various layers in the tandem. The PL measurement would then detect this as a bright spot in the CIGSe device, since the ohmic shunt is across the whole tandem.

When it comes to cracking of the perovskite film, it is also interesting to see that other than some mild wrinkles, the champion, 23.1%-efficient device also has a crack around the P1 scribe under the Ag ring, right at the border with the active area. This crack is the only detected defect on the champion device and it could have appeared because of the scribing of the tandems (zoomed-out view in the left-most figure at figure 10(b) indicates that the P1 scribe could be problematic), or because of the needles that are placed on the Ag ring during the *JV* measurements of the tandem.

3. Conclusion and outlook

In this paper we investigated how the HTL, the bottom, or the top device affect the FF and the shunts formation in monolithic CIGSe-perovskite tandem solar cells. To disentangle the influence of each of these parameters, we adopted a variety of characterization techniques, such as photoelectron spectroscopy (XPS/UPS) and EDX measurements of the HTL on the one hand, and current density–voltage (*JV*) measurements and extensive imaging (DLIT, PL, and SEM) of the complete tandem devices on the other hand. We presented results for eight tandems with four different HTL configurations—air- or N_2 -transferred NiO_x with or without SAM. Despite the small statistics, the two devices per each HTL configuration displayed comparable performance and enabled us to distinguish the main source for the FF losses, as summarized in table 3 below.

In absence of ohmic shunts, PL-detected defects in the bottom device, and macroscopic defects in the top device, observed losses in the FF are most likely caused by the HTL. This is most prominently displayed by the tandems with air-transferred $\text{NiO}_x\text{:Cu}$ without SAM. The XPS measurements indicated that due to an increase in the amount of hydroxides, the 24 h long air exposure leads to $\sim 11\%$ less Ni^{2+} concentration on the $\text{NiO}_x\text{:Cu}$ surface compared to the 24 h long N_2 exposure. The UPS measurements indicate that the air exposure can also lead to changes in the VBM and the WF of the $\text{NiO}_x\text{:Cu}$. These effects likely lead to an increased charge-trapping, redox reactions, and a less favorable band alignment at the $\text{NiO}_x\text{:Cu}$ -perovskite interface. Passivating the $\text{NiO}_x\text{:Cu}$ surface with SAM is then argued to diminish the trapping and improves the band alignment at the $\text{NiO}_x\text{:Cu}$ -perovskite interface, yielding highly performing CIGSe-perovskite tandem solar cells. This effect is more prominent with the N_2 -transferred $\text{NiO}_x\text{:Cu}$ due to a slower N_2^{2+} decay in the inert atmosphere.

For an N_2 -transferred $\text{NiO}_x\text{:Cu}$, which has no prominent loss in the Ni^{2+} concentration, as well as a defect-free top device, a correlation between PL-detected defects in the bottom device and a DLIT-detected location of the ohmic shunts enables us to ascribe the source of the FF loss to the bottom device.

On the devices where SAM surface passivation of the HTL was adopted, the shunting is unlikely to originate from the HTL. Here, SEM detection of cracking and lift-off in the top device layer stack also causes DLIT-detected ohmic shunt(s), ascribing the main FF losses to the perovskite.

Finally, the tandem devices with N_2 -transferred $\text{NiO}_x\text{:Cu}$ + SAM are highly-performing (22%–23%) because the N_2 -transferred $\text{NiO}_x\text{:Cu}$ has less Ni^{2+} vacancies that the SAM needs to passivate as well as because both the bottom and the top device are free of macroscopic defects. Moreover, the FF for these devices is boosted by the current mismatch in the monolithic tandems, which can be confirmed by performing *JV* measurements with varying amounts of blue and red light.

Table 3. Summary of the detected defects in the finished tandem devices alongside the variations in the HTL configuration and their power-conversion efficiency.

HTL	NiO _x :Cu (air)	NiO _x :Cu (N ₂)	NiO _x :Cu (air) + SAM	NiO _x :Cu (N ₂) + SAM
PCE (%)	10–11	~6	~17	22–23
Heat dissipation	Yes	Negligible	Yes	Negligible
Non-linear shunts	Yes	Yes	No	No
Ohmic shunts	No	Yes, many	Yes, one	No
PL-ohmic shunts correlation	No	Yes	Yes	No
Breaking of perovskite FF loss	No	No	Yes	No
caused by:	HTL	CIGSe	perovskite	no shunts

We show that detecting the inception point of the shunts in monolithic CIGSe-perovskite tandems solar cells requires a combination of various characterization methods due to the complex monolithic stack in which each component can induce changes in the layers and the interfaces above and below. We found that the rough and defect-rich CIGSe surface is not always the main culprit for the shunting in monolithic CIGSe-perovskite tandems and that the processing environment of the HTL and/or the top device can also induce shunts and thus FF losses in the complete tandem device. Moreover, we show that not all PL-detected defects in the bottom device induce ohmic shunts and FF losses in the complete tandems. This is an important finding because it indicates that the NiO_x:Cu enables us to decouple the growth of the top device from the bottom device by insulating defects in the bottom device, thus enabling us to prepare a shunt-free top and tandem device. This finding is a first step toward more reproducible results and higher yield for the CIGSe-perovskite monolithic tandem devices prepared on rough CIGSe absorbers, especially as the research might try to progress to rougher CIGSe surfaces and larger tandem cells' areas.

Therefore, as a future outlook one should explore strategies to avoid stress-induced breaking of the perovskite film, for example by omitting the P1 scribe and depositing the AZO through a mask. During the spin coating of the perovskite absorber, the anti-solvent should be dropped closer to the sample to avoid extra stress due to possible splashing. For larger areas, other deposition techniques of the perovskite top-cell absorber beyond spin coating should be also explored. On the CIGSe side, one should use not only a high quality CIGSe, but also ensure that the AZO surface is clean and free of glass particles when cutting the samples to the required size for the processing of the tandem devices.

4. Experimental

4.1. Samples preparation

The single-junction solar cells are manufactured on patterned ITO cleaned for 15 min in an ultrasonic bath with soap, DI water, acetone, and isopropanol, and then in a UV-O₃ cleaner. The substrate for the CIGSe absorber is a 5 by 5 cm² 1 mm-thick soda-lime glass on top of which a molybdenum (Mo) back contact (~800 nm) is deposited via a direct-current (DC) magnetron sputtering. The CIGSe absorber is co-evaporated in a three-stage process [56] and is subjected to a RbF post-deposition treatment [57]. The fina ratio of [Ga] to [Ga] + [In] amount (GGI) ratio is ~1.09 and the E_g ~ 1.12 eV. Then, the samples are dipped into a 60 °C heated solution of deionized (DI) water and Cd-acetate (2.5 mM, purity >98%), thiourea (0.05 M, purity >99%) and aqueous ammonia solution (max. contamination ≤260 ppm, the ammonia is GPR RECTAPUR) until a 60 nm-thick CdS is grown [58]. RF sputtering is used to deposit the intrinsic (i-ZO, 40 nm) and the aluminum-doped (AZO, 60 nm) zinc oxide. P1 laser scribing is used to define what later becomes an active area for the monolithic tandem. The 5 by 5 cm² substrate is then cut into 2.54 by 2.54 cm² samples which are then directly taken for the NiO_x:Cu sputtering.

The NiO_x:Cu (10 nm) layers are RF-sputtered from a NiO_x:Cu target (2%Cu, Nova Fabrica) in pure Ar (99.999%) atmosphere, with no intentional heating beyond the heating provided by the plasma, at a power of 60 W, pressure of $(4.6 \pm 0.1) \times 10^{-3}$ mbar, ≈ 5 cm target-to sample distance, and at a constant sputtering bias of ≈230 V. After the sputtering, the samples are either transferred to and sealed in a N₂-filled glovebox; or, they are exposed to air. The samples that undergo N₂ transfer and have NiO_x:Cu as a stand-alone HTL are transferred to another N₂-filled glovebox for the perovskite deposition. The total exposure time to N₂ was around one to two hours before the perovskite is deposited.

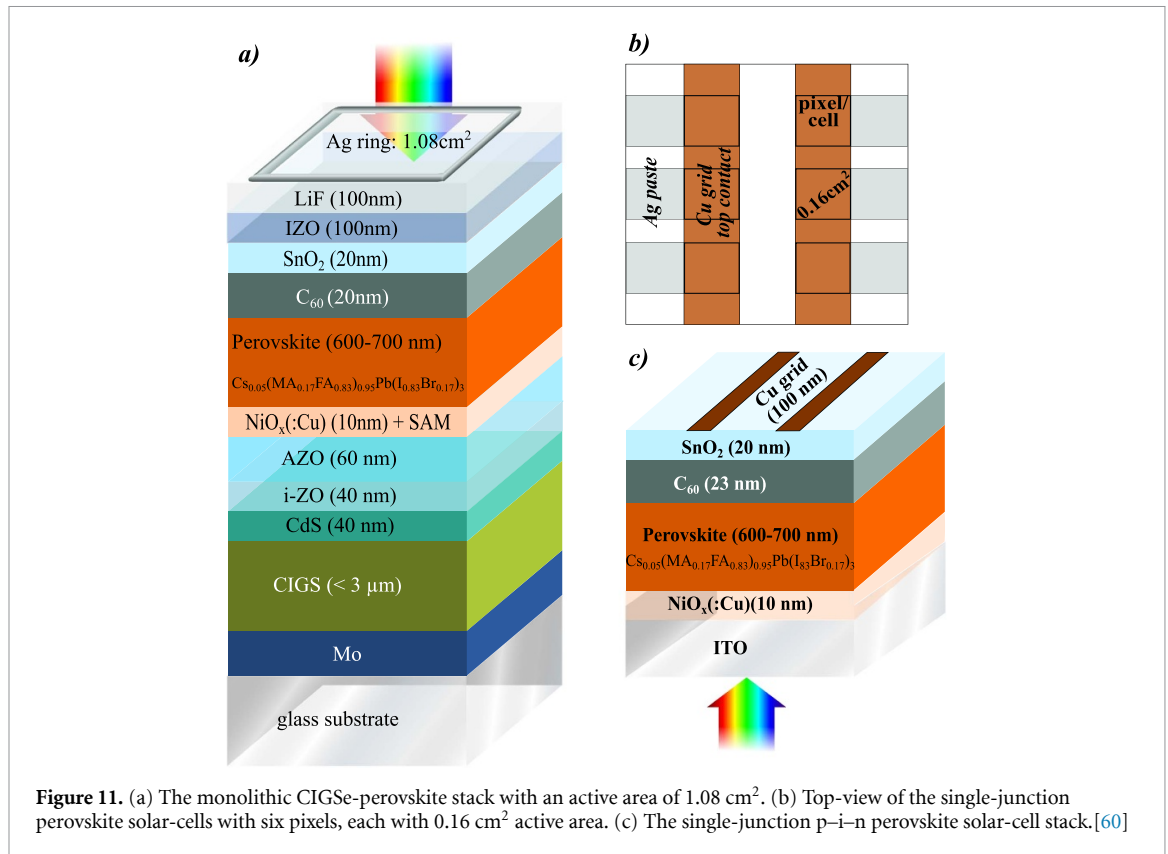


Figure 11. (a) The monolithic CIGSe-perovskite stack with an active area of 1.08 cm². (b) Top-view of the single-junction perovskite solar-cells with six pixels, each with 0.16 cm² active area. (c) The single-junction p–i–n perovskite solar-cell stack. [60]

The samples with SAM (MeO-2PACz ([2-(3,6-dimethoxy-9H-carbazol-9-yl) ethyl]phosphonic acid)) are exposed to a 15 min O₃ treatment in a UV-O₃ cleaner prior to the SAM deposition. The UV light is blocked by a glass panel. MeO-2PACz powder (>98% purity, TCI) is mixed with anhydrous ethanol (VWR chemical) to obtain a 1 mM solution, after which 100 μl of the solution are spin-coated at 4000 rps for 45 s and subsequently annealed at 100 °C for 10 min.

Next, the perovskite (Cs_{0.05}(MA_{0.17}FA_{0.83})_{0.95}Pb(I_{0.83}Br_{0.17})₃ (CsMAFA), E_g = 1.63 eV [59]) is deposited by spin-coating a 100 μl of a perovskite precursor solution at 4000 rpm for 40 s (out of which 5 s are acceleration). As anti-solvent, 500 μl of ethyl acetate (anhydrous, 99.8% purity, Sigma Aldrich manufacturer) is used. The perovskite deposited for the single junctions is annealed at 100 °C for an hour and for the tandems for 1 h.

The perovskite precursor solution is prepared in several steps. First, PbI₂ and PbBr₂ salts (both with 99.99% purity, TCI manufacturer) are dissolved by a 4:1 ratio DMF:DMSO solution (DMF: N,N-dimethylformamide, DMSO: dimethylsulfoxid, Sigma-Aldrich manufacturer). The PbI₂ and PbBr₂ mixtures are shaken overnight (T = 60 °C). The next day, the PbI₂ and PbBr₂ solutions are used to dissolve a FAI (formamidinium iodide, 99.99% purity, dyenamo manufacturer) and a MABr (methylammonium bromide, 99.99% purity, dyenamo manufacturer) salt, respectively. The FAPbI₃ (formamidinium lead iodide) and MAPbBr₃ (methylammonium lead bromide) solutions are mixed into one solution with a CsI solution (cesium iodide, 99.999% Cs and DMSO as a solvent) with the ratios presented in [59] to produce a final triple-cation perovskite precursor solution.

The top cell is finalized by evaporating C₆₀ (23 nm for the single junctions and 20 nm for the tandems) and ALD SnO₂ (20 nm at 80 °C via 140 cycles). The single junctions are finalized by evaporating a copper (Cu) grid (100 nm), while the tandems receive a sputtered Indium-Zinc-Oxide (IZO) (100 nm), and evaporated silver (Ag) ring (2 * 100 nm) to mark a 1.08 cm² active area of the tandem. Lithium fluoride (LiF) is evaporated (100 nm) as an anti-reflective coating. A schematic of the single-junction and tandem devices is shown in figure 11.

4.2. Characterization techniques

For the *current density-voltage (JV)* measurements of the tandem devices a 12 LED Sun simulator (Wavelabs manufacturer, class AAA) calibrated with a KG3 silicon reference cell was used. The measurements were performed in air at a temperature of 25 °C. For the single-junction JV measurements in an N₂ environment an Oriel class ABB Sun simulator under a simulated illumination of an AM 1.5G spectrum was

used. No light-soaking or biasing is used. The cells were measured in both a forward-bias ($V_{\text{start}} < V_{\text{end}}$) and in reverse-bias ($V_{\text{start}} > V_{\text{end}}$) scan direction.

For the EQE measurements a three-LED (blue, red, green) set-up was used. A 300 nm–770 nm and 500 nm–1250 nm wavelength ranges, in steps of 10 nm, were used for probing the perovskite and the CIGSe cell, respectively. The small-spot reflection (R) measurements were done with a PerkinElmer Lambda 1050 dual-beam photometer with an integrating sphere in the spectral range from 300 nm to 1250 nm, in 10 nm steps.

For the XPS measurements, XR-50 x-ray source (SPECS) with a Mg $K\alpha$ (1253.6 eV) at a power of 150 W and a CLAM 4 electron analyser vacuum generator (VG) is used. The pass energy is 20 eV. For the UPS measurements a UV HeI (21.2 eV) source and a 2.5 eV pass energy are used. The XPS/UPS analytic chamber is connected to both the sputtering chamber and to a loadlock with two exit stations: to air and to an N_2 -filled glovebox. Therefore, the reference XPS/UPS measurements of the NiO_x :Cu films deposited either on ITO or CIGSe cell are obtained by transferring the samples from the sputter chamber to the XPS/UPS analytic chamber without breaking vacuum, right after sputtering. The samples exposed to air are taken out throughout the loadlock and the samples exposed to N_2 are moved to the glovebox. For details on the sputtering and XPS/UPS setup, refer to [61].

The SEM and EDX measurements were performed in the same system. The SEM is a Zeiss Merlin FE-SEM, while the EDX detector is a Bruker XFlash 6/100. The SEM images were obtained at varying magnification (written under the respective image in the Results section or in the supplementary information) at accelerating voltages of 2–4 keV. The EDX images are obtained at two different voltages: 4 keV and 15 keV and varying magnifications. All SEM images and EDX compositional maps and spectra are obtained as a top-view (not cross-sectional) imaging of the samples.

The DLIT imaging is performed on the finished tandem devices in a high-resolution Thermosensorik system equipped with a ‘TDL 640’ InSb mid-wave infrared (MWIR) camera with a focal length of 28 mm [62]. Since the thermal diffusion length (TDL) of the thermal waves within the materials is inversely proportional to the frequency of the injection ($TDL \propto 1/\sqrt{f_{\text{lock-in}}}$), higher $f_{\text{lock-in}}$ yields higher spatial resolution [50]. Additionally, the measurement time (i.e. the number of lock-in periods throughout the measurements) is inversely proportional to the amplitude of the average noise ($A_{\text{noise}} \propto 1/\sqrt{t_{\text{meas}}}$), meaning that longer measurements should yield better signal-to-noise ratio [50]. Taking these two relations into consideration, the high-injection DLIT images presented in this work are obtained at two different frequencies and times (1 Hz and 1 min, and 10 Hz and 5 min).

The PL imaging is performed with an InGaAs camera (measuring from 0.9 to 1.7 μm) with a 650 nm excitation wavelength at an integration time from 15 to 300 ms. The used software was LumiSolarMobile System (GreatEyes).

Data availability statement

The data cannot be made publicly available upon publication due to legal restrictions preventing unrestricted public distribution. The data that support the findings of this study are available upon reasonable request from the authors.

Acknowledgments

Funding was provided by the Federal Ministry of Economy and Energy (Bundesministerium für Wirtschaft und Energie) for the speedCIGS project (Grant No. 0324095D). The authors further acknowledge S Albrecht and A Al-Ashouri, the HySPRINT Lab at Helmholtz-Zentrum Berlin and HyPerCells—a joint graduate school of the University of Potsdam and the Helmholtz-Zentrum Berlin. The authors also thank T Hänel, B Bunn, J Lauche, T Münchenberg, E Waack, R Haberecht, A Steigert, K Mayer-Stillrich, M Hartig, M Kirsch, N El-Ganainy, and M Wittig for technical support during device fabrication.

ORCID iDs

I Kafedjiska  <https://orcid.org/0000-0002-4088-4221>

G Farias Basulto  <https://orcid.org/0000-0002-8419-1494>

F Ruske  <https://orcid.org/0000-0002-6363-4591>

N Maticiuc  <https://orcid.org/0000-0002-5654-3560>

T Bertram  <https://orcid.org/0000-0002-4060-7523>

C A Kaufmann  <https://orcid.org/0000-0001-9168-2032>

R Schlatmann  <https://orcid.org/0000-0002-5951-9435>

I Lauer mann  <https://orcid.org/0000-0002-9119-3770>

References

- [1] Shockley W and Queisser H J 1961 Detailed balance limit of efficiency of p-n junction solar cells *J. Appl. Phys.* **32** 510–9
- [2] Al-Ashouri A et al 2019 Conformal monolayer contacts with lossless interfaces for perovskite single junction and monolithic tandem solar cells *Energy Environ. Sci.* **12** 3356–69
- [3] Al-Ashouri A et al 2020 Monolithic perovskite/silicon tandem solar cell with >29% efficiency by enhanced hole extraction *Science* **370** 1300–9
- [4] Best Research-Cell Efficiency Chart 2021 (available at: www.nrel.gov/pv/cell-efficiency.html)
- [5] Jošt M 2022 Perovskite/CIGS tandem solar cells: from certified 24.2% toward 30% and beyond *ACS Energy Lett.* **7** 1298–307
- [6] Ramanujam J and Singh U P 2017 Copper indium gallium selenide based solar cells—a review *Energy Environ. Sci.* **10** 1306–19
- [7] Kim D, Shin S S, Lee S M, Cho J-S, Yun J H, Lee H S and Park J H 2020 Flexible and semi-transparent ultra-thin CIGSe solar cells prepared on ultra-thin glass substrate: a key to flexible bifacial photovoltaic applications *Adv. Funct. Mater.* **30** 2001775
- [8] Caballero R, Kaufmann C A, Eisenbarth T, Unold T, Klenk R and Schock H-W 2011 High efficiency low temperature grown Cu(In,Ga)Se₂ thin film solar cells on flexible substrates using NaF precursor layers *Prog. Photovolt., Res. Appl.* **19** 547–51
- [9] Ruiz-Preciado M A et al 2022 Monolithic two-terminal perovskite/CIS tandem solar cells with efficiency approaching 25% *ACS Energy Lett.* **7** 2273–81
- [10] Nakamura M, Yamaguchi K, Kimoto Y, Yasaki Y, Kato T and Sugimoto H 2019 Cd-free Cu(In,Ga)(Se,S)₂ thin-film solar cell with record efficiency of 23.35% *IEEE J. Photovolt.* **9** 1863–7
- [11] Jošt M et al 2019 21.6%-efficient monolithic perovskite/Cu(In,Ga)Se₂ tandem solar cells with thin conformal hole transport layers for integration on rough bottom cell surfaces *ACS Energy Lett.* **4** 583–90
- [12] Guo X, Luo G, Liu J, Liao C, Wang G and Li S 2018 A 16.5% efficient perovskite solar cells with inorganic NiO film as hole transport material *IEEE J. Photovolt.* **8** 1039–43
- [13] Zhang H, Cheng J, Lin F, He H, Mao J, Wong K S, Jen A K-Y and Choy W C H 2016 Pinhole-free and surface-nanostructured NiO_x film by room-temperature solution process for high-performance flexible perovskite solar cells with good stability and reproducibility *ACS Nano* **10** 1503–11
- [14] Di Girolamo D, Di Giacomo F, Matteocci F, Marrani A G, Dini D and Abate A 2020 Progress, highlights and perspectives on NiO in perovskite photovoltaics *Chem. Sci.* **11** 7746–59
- [15] Li G, Jiang Y, Deng S, Tam A, Xu P, Wong M and Kwok H-S 2017 Overcoming the limitations of sputtered nickel oxide for high-efficiency and large-area perovskite solar cells *Adv. Sci.* **4** 1700463
- [16] Aydin E et al 2018 Room-temperature-sputtered nanocrystalline nickel oxide as hole transport layer for p-i-n perovskite solar cells *ACS Appl. Energy Mater.* **1** 6227–33
- [17] Pang S, Zhang C, Dong H, Chen D, Zhu W, Xi H, Chang J, Lin Z, Zhang J and Hao Y 2019 Efficient NiO_x hole transporting layer obtained by the oxidation of metal nickel film for perovskite solar cells *ACS Appl. Energy Mater.* **2** 4700–7
- [18] Abzieher T et al 2019 Electron-beam-evaporated nickel oxide hole transport layers for perovskite-based photovoltaics *Adv. Energy Mater.* **9** 1802995
- [19] Zhao B et al 2018 *In situ* atmospheric deposition of ultrasmooth nickel oxide for efficient perovskite solar cells *ACS Appl. Mater. Interfaces* **10** 41849–54
- [20] Koushik D, Jošt M, Dučinskas A, Burgess C, Zardetto V, Weijtens C, Verheijen M A, Kessels W M M, Albrecht S and Creatore M 2019 Plasma-assisted atomic layer deposition of nickel oxide as hole transport layer for hybrid perovskite solar cells *J. Mater. Chem.* **7** 12532–43
- [21] Kavadiya S, Onno A, Boyd C C, Wang X, Cetta A, McGehee M D and Holman Z C 2021 Investigation of the selectivity of carrier transport layers in wide-bandgap perovskite solar cells *Solar RRL* **5** 2100107
- [22] Pant N, Yanagida M, Shirai Y and Miyano K 2020 Effect of different surface treatments of sputtered NiO_x on the photovoltaic parameters of perovskite solar cells: a correlation study *Appl. Phys. Express* **13** 025505
- [23] Pant N, Kulkarni A, Yanagida M, Shirai Y, Miyasaka T and Miyano K 2020 Investigating the growth of CH₃NH₃PbI₃ thin films on rf-sputtered NiO_x for inverted planar perovskite solar cells: effect of CH₃NH₃⁺ halide additives versus CH₃NH₃⁺ halide vapor annealing *Adv. Mater. Interfaces* **7** 1901748
- [24] Pant N, Kulkarni A, Yanagida M, Shirai Y, Miyasaka T and Miyano K 2020 Residual PbI₂ beneficial in the bulk or at the interface? An investigation study in sputtered NiO_x hole-transport-layer-based perovskite solar cells *ACS Appl. Energy Mater.* **3** 6215–21
- [25] Boyd C C et al 2020 Overcoming redox reactions at perovskite-nickel oxide interfaces to boost voltages in perovskite solar cells *Joule* **4** 1759–75
- [26] Chen W et al 2018 Understanding the doping effect on NiO: toward high-performance inverted perovskite solar cells *Adv. Energy Mater.* **8** 1703519
- [27] Zheng X et al 2020 Interface modification of sputtered NiO_x as the hole-transporting layer for efficient inverted planar perovskite solar cells *J. Mater. Chem. C* **8** 1972–80
- [28] Pant N, Kulkarni A, Yanagida M, Shirai Y, Yashiro S, Sumiya M, Miyasaka T and Miyano K 2021 Passivation of bulk and interface defects in sputtered-NiO_x-based planar perovskite solar cells: a facile interfacial engineering strategy with alkali metal halide salts *ACS Appl. Energy Mater.* **4** 4530–40
- [29] Di Girolamo D et al 2019 Stability and dark hysteresis correlate in NiO-based perovskite solar cells *Adv. Energy Mater.* **9** 1901642
- [30] Subbiah A S et al 2020 High-performance perovskite single-junction and textured perovskite/silicon tandem solar cells via slot-die-coating *ACS Energy Lett.* **5** 3034–40
- [31] Hou Y et al 2020 Efficient tandem solar cells with solution-processed perovskite on textured crystalline silicon *Science* **367** 1135–40
- [32] Phung N et al 2022 Enhanced self-assembled monolayer surface coverage by ALD NiO in p-i-n perovskite solar cells *ACS Appl. Mater. Interfaces* **14** 2166–76
- [33] Fellmeth T, Clement F and Biro D 2014 Analytical modeling of industrial-related silicon solar cells *IEEE J. Photovolt.* **4** 504–13
- [34] McMahon W E, Emery K E, Friedman D J, Ottoson L, Young M S, Ward J S, Kramer C M, Duda A and Kurtz S 2008 Fill factor as a probe of current-matching for GaInP₂/GaAs tandem cells in a concentrator system during outdoor operation *Prog. Photovolt., Res. Appl.* **16** 213–24

- [35] Ulbrich C, Zahren C, Gerber A, Blank B, Merdzhanova T, Gordijn A and Rau U 2013 Matching of silicon thin-film tandem solar cells for maximum power output *Int. J. Photoenergy* **2013** e314097
- [36] Köhnen E et al 2019 Highly efficient monolithic perovskite silicon tandem solar cells: analyzing the influence of current mismatch on device performance *Sustain. Energy Fuels* **3** 1995–2005
- [37] Ratcliff E L, Meyer J, Steirer K X, Garcia A, Berry J J, Ginley D S, Olson D C, Kahn A and Armstrong N R 2011 Evidence for near-Surface NiOOH species in solution-processed NiO_x selective interlayer materials: impact on energetics and the performance of polymer bulk heterojunction photovoltaics *Chem. Mater.* **23** 4988–5000
- [38] Zhang Y, Yang M, Du J, Yang L, Fan L, Liu X, Yang J and Wang F 2019 Modulation of Ni³⁺ and crystallization of dopant-free NiO_x hole transporting layer for efficient p-i-n perovskite solar cells *Electrochim. Acta* **319** 41–48
- [39] Grosvenor A P, Biesinger M C, Smart R S and McIntyre N S 2006 New interpretations of XPS spectra of nickel metal and oxides *Surf. Sci.* **600** 1771–9
- [40] Corani A, Li M-H, Shen P-S, Chen P, Guo T-F, El Nahhas A, Zheng K, Yartsev A, Sundström V and Ponceca C S 2016 Ultrafast dynamics of hole injection and recombination in organometal halide perovskite using nickel oxide as p-type contact electrode *J. Phys. Chem. Lett.* **7** 1096–101
- [41] Tiwari N, Arianita Dewi H, Erdenebileg E, Narayan Chauhan R, Mathews N, Mhaisalkar S and Bruno A 2022 Advances and potentials of NiO_x surface treatments for p-i-n perovskite solar cells *Solar RRL* **6** 2100700
- [42] Boyd C C, Checharoen R, Leijtens T and McGehee M D 2019 Understanding degradation mechanisms and improving stability of perovskite photovoltaics *Chem. Rev.* **119** 3418–51
- [43] Khodabakhsh S, Poplavskyy D, Heutz S, Nelson J, Bradley D D C, Murata H and Jones T S 2004 Using self-assembling dipole molecules to improve hole injection in conjugated polymers *Adv. Funct. Mater.* **14** 1205–10
- [44] Hotchkiss P J, Li H, Paramonov P B, Paniagua S A, Jones S C, Armstrong N R, Brédas J-L and Marder S R 2009 Modification of the surface properties of indium tin oxide with benzylphosphonic acids: a joint experimental and theoretical study *Adv. Mater.* **21** 4496–501
- [45] Ogomi Y, Morita A, Tsukamoto S, Saitho T, Shen Q, Toyoda T, Yoshino K, Pandey S S, Ma T and Hayase S 2014 All-solid perovskite solar cells with HOCO-R-NH₃⁺I⁻ anchor-group inserted between porous titania and perovskite *J. Phys. Chem. C* **118** 16651–59
- [46] Wojciechowski K et al 2014 Heterojunction modification for highly efficient organic-inorganic perovskite solar cells *ACS Nano* **8** 12701–9
- [47] Bin Kim H, Im I, Yoon Y, Do Sung S, Kim E, Kim J and In Lee W 2015 Enhancement of photovoltaic properties of CH₃NH₃PbBr₃ heterojunction solar cells by modifying mesoporous TiO₂ surfaces with carboxyl groups *J. Mater. Chem. A* **3** 9264–70
- [48] Liu K, Chen S, Wu J, Zhang H, Qin M, Lu X, Tu Y, Meng Q and Zhan X 2018 Fullerene derivative anchored SnO₂ for high-performance perovskite solar cells *Energy Environ. Sci.* **11** 3463–71
- [49] Will J, Hou Y, Scheiner S, Pinkert U, Hermes I M, Weber S A L, Hirsch A, Halik M, Brabec C and Unruh T 2018 Evidence of tailoring the interfacial chemical composition in normal structure hybrid organohalide perovskites by a self-assembled monolayer *ACS Appl. Mater. Interfaces* **10** 5511–8
- [50] Bauer J, Breitenstein O and Wagner J-M 2009 Lock-in thermography: a versatile tool for failure analysis of solar cells *Electron. Device Fail. Anal.* **11** 6–12
- [51] Breitenstein O 2013 Illuminated versus dark lock-in thermography investigations of solar cells *Int. J. Nanoparticles* **6** 81–92
- [52] Ramspeck K, Bothe K, Hinken D, Fischer B, Schmidt J and Brendel R 2007 Recombination current and series resistance imaging of solar cells by combined luminescence and lock-in thermography *Appl. Phys. Lett.* **90** 153502
- [53] Breitenstein O and Rakotoniaina J P 2005 Electrothermal simulation of a defect in a solar cell *J. Appl. Phys.* **97** 074905
- [54] Wang S-Y, Chen C-P, Chung C-L, Hsu C-W, Hsu H-L, Wu T-H, Zhuang J-Y, Chang C-J, Chen H M and Chang Y J 2019 Defect passivation by amide-based hole-transporting interfacial layer enhanced perovskite grain growth for efficient p-i-n perovskite solar cells *ACS Appl. Mater. Interfaces* **11** 40050–61
- [55] Kim S-G, Kim J-H, Ramming P, Zhong Y, Schötz K, Kwon S J, Huettner S, Panzer F and Park N-G 2021 How antisolvent miscibility affects perovskite film wrinkling and photovoltaic properties *Nat. Commun.* **12** 1554
- [56] Heinemann M D, Mainz R, Österle F, Rodriguez-Alvarez H, Greiner D, Kaufmann C A and Unold T 2017 Evolution of opto-electronic properties during film formation of complex semiconductors *Sci. Rep.* **7** 45463
- [57] Kodalle T, Heinemann M D, Greiner D, Yetkin H A, Klupsch M, Li C, van Aken P A, Lauer mann I, Schlattmann R and Kaufmann C A 2018 Elucidating the mechanism of an RbF post deposition treatment in CIGS thin film solar cells *Solar RRL* **2** 1800156
- [58] Ortega-Borges R and Lincot D 1993 Mechanism of chemical bath deposition of cadmium sulfide thin films in the ammonia-thiourea system: in situ kinetic study and modelization *J. Electrochem. Soc.* **140** 3464
- [59] Saliba M et al 2016 Cesium-containing triple cation perovskite solar cells: improved stability, reproducibility and high efficiency *Energy Environ. Sci.* **9** 1989–97
- [60] Kafedjiska I, Farias-Basulto G A, Reyes-Figueroa P, Bertram T, Al-Ashouri A, Kaufmann C A, Wenisch R, Albrecht S, Schlattmann R and Lauer mann I 2023 Integration of rough RTP absorbers into CIGS-perovskite monolithic tandems by NiO_x(:Cu)+SAM Hole-transporting Bi-layers *Solar Energy Materials and Solar Cells* **254** 112248
- [61] Lauer mann I and Steigert A 2016 CISSY: a station for preparation and surface/interface analysis of thin film materials and devices *J. Large-Scale Res. Facil.* **2** 67
- [62] PVcomB - Lock-In 2022 Helmholtz-zentrum berlin für materialien und energie (available at: www.helmholtz-berlin.de/projects/pvcomb/analytik/lit_en.html)